

# A landslide runout model for sediment transport, landscape evolution and hazard assessment applications

Jeffrey Keck<sup>1,2</sup>, Erkan Istanbuluoglu<sup>1</sup>, Benjamin Campforts<sup>3</sup>, Gregory Tucker<sup>4,5</sup>, Alexander Horner-Devine<sup>1</sup>

<sup>1</sup> University of Washington, Civil and Environmental Engineering, Seattle, WA, USA

<sup>2</sup> Washington Department of Natural Resources, Forest Resources Division, Olympia, WA, USA

<sup>3</sup> [Department of Earth Sciences, Vrije University, Amsterdam, Netherlands](#) ~~Institute of Arctic and Alpine Research, University of Colorado Boulder, Boulder, CO, USA~~

<sup>4</sup> Department of Geological Sciences, University of Colorado Boulder, Boulder, CO, USA

<sup>5</sup> Cooperative Institute for Research in Environmental Sciences (CIRES), University of Colorado Boulder, Boulder, CO, USA

*Correspondence to:* Jeffrey Keck (keckje@gmail.com)

## Abstract

We developed a new rule-based, cellular-automaton algorithm for predicting the hazard extent, sediment transport and topographic change associated with the runout of a landslide. This algorithm, which we call MassWastingRunout (MWR), is coded in Python and implemented as a component for the package Landlab. MWR combines the functionality of simple runout algorithms used in landscape evolution and watershed sediment yield models with the predictive details typical of runout models used for landslide inundation hazard mapping. An initial DEM, a regolith depth map, and the location polygon of ~~a~~ the landslide source area are the only inputs required to run MWR to model the entire runout process. ~~MWR runout incorporates~~ Runout relies on the principle of rules of mass conservation and a set of topographic rules and empirical formulas that govern erosion and deposition, ~~which are driven by topography~~. For the purpose of facilitating rapid calibration to a site, MWR includes a calibration utility that uses a Markov Chain Monte Carlo algorithm to automatically calibrate the model to match observed runout extent, deposition and erosion. ~~Output~~ Additionally, from the calibration utility produces empirical probability density functions of each calibration parameter that can be used to inform probabilistic implementation of MWR. Here we use a series of synthetic terrains to demonstrate basic model response to topographic convergence and slope, test calibrated model performance relative to several observed landslides, and briefly demonstrate how MWR can be used to develop a probabilistic runout hazard map. A calibrated runout model may allow for region-specific and more insightful predictions of landslide impact on landscape morphology and watershed-scale sediment dynamics, and should be further investigated in future modelling studies.

## 1. Introduction

Over geologic timescales, landslides and their runout shape the topographic expression of mountain ranges and channel networks (e.g., Campforts et al., 2022; Korup, 2006; Larsen and Montgomery, 2012; Montgomery and Dietrich, 1988). Over more pragmatic engineering and environmental risk management timescales, landslides and

36 their runout can inundate and destroy infrastructure (e.g., Kean et al., 2019) but also support numerous ecosystem  
37 benefits, including carbon and nutrient transport from hillslopes to channels and the creation of riparian habitat (Benda  
38 et al., 2003; Bigelow et al., 2007; Goode et al., 2012). Therefore, explicit representation of landslide runout is a  
39 necessary component of: (1) landslide inundation hazard assessments, with emphasis on inundation extent and flow  
40 depth (e.g., Frank et al. 2015, Han et al., 2015); (2) watershed sediment yield models, with emphasis on the  
41 mobilization, deposition and type of sediment carried by the landslide (e.g., Bathurst and Burton, 1998;  
42 Istanbuluoglu, et al., 2005); and (3) landscape evolution models, with emphasis on topographic change prediction  
43 (e.g., Tucker and Bras, 1998; Istanbuluoglu and Bras, 2005; Campforts et al., 2022);

44 Landslide runout processes can be generalized into three phases: initiation, erosion, and deposition. After a landslide  
45 initiates, it may break apart and flow as a relatively dry debris slide, or it may mix with surface runoff to become a  
46 debris flow. The mobility of the mass wasting material and resulting erosion/deposition pattern often varies as a  
47 function of runout topography and initial relief and size of the landslide (Iverson, 1997). Mobility may also be  
48 impacted by substrate liquefaction (Hung and Evans, 2004) and landslide basal cataclasis (Shaller et al. 2020). As  
49 the runout material moves downslope, flow depth varies as a function of channel width (Kean et al, 2019), which in  
50 turn impacts erosion rates (Schürch et al. 2011). Theoretical, field and laboratory observations indicate that erosion  
51 rates may also depend on the moisture content of the channel bed (Iverson, 2012; McCoy et al. 2012), flow grainsize  
52 (Egashira et al., 2001) and granular stress within the flow (Capart et al, 2015). The slope at which deposition begins  
53 is controlled by the grain to water ratio and friction angle of the slide material (Takahashi, 2014; Major and Iverson,  
54 1999; Zhou et al., 2019) but the friction angle of the material may vary as a function of the grains in the flow and  
55 fluidization of the flow material (Hutter et al., 1996). Lateral levees often form along the edges of the flow (Major,  
56 1997; Whipple and Dunne, 1992; Shaller et al., 2020) and deposition at the distal end of the flow may occur as layered  
57 accretion (Major, 1997) or as the emplacement of a single, massive deposit (Shaller et al., 2020). If the water content  
58 of the runout material is high enough, as the solid fraction of the distal end of the flow compresses, the water is  
59 squeezed out and may continue as an immature debris flow (sensu Takahashi, 2014) or intense bedload (sensu Capart  
60 & Fraccarolo, 2011), extending the runout distance (e.g., Shaller et al. 2020).

61 Landslide inundation hazard models aim to accurately predict the runout extent and/or flow depths of a runout event  
62 and may include some or most of the above processes in the model. Example models include: (1) site-specific-  
63 empirical/statistical models that use simple geometric rules and an estimate of the total mobilized volume (initial  
64 landslide + eroded volume) or a growth factor (e.g., Reid et al. 2016); (2) detailed, continuum-based mechanistic  
65 models, which conceptualize the runout process as a single-phase or multiphase flow using the depth-integrated  
66 Navier-Stokes equations for an incompressible, free-surface flow (i.e., shallow water equations; Frank et al, 2015;  
67 Han et al., 2015; Iverson and Denlinger, 2001; [Medina et al., 2008](#)) and often (though not always) require pre-  
68 knowledge of the total mobilized volume (e.g., Barnhart et al., 2021; Han et al. 2015); (3) reduced-complexity flow-  
69 routing models that use rule-based abstractions of the key physical processes that control the flow (Clerici and Perego,  
70 2000; Guthrie and Befus, 2021; Gorr et al., 2022; Han et al., 2017, 2021; Horton et al., 2013; Liu et al, 2022) and are  
71 typically implemented using just the initial landslide location and volume but often rely on heavy, site specific  
72 parameterization and; (4) hybrid modelling approaches that combine mechanistic models with empirical and reduced

73 –complexity approaches (D’Ambrosio et al., 2003; Iovine et al., 2005; Lancaster et al., 2003; McDougall and Hungr  
74 2004; [Medina et al., 2008](#)).

75 For landscape evolution and watershed sediment yield applications (herein referred to as watershed sediment models,  
76 WSMs), the runout model must be scalable in both space and time, and [capable of modelling the entire runout process](#)  
77 [given an](#)use internally modelled [initial](#) landslide [location and size](#) [body](#) (e.g. Tucker and Bras, 1998; Doten et al 2006;  
78 Campforts et al. 2022). As such, computationally efficient and parsimonious reduced complexity runout models that  
79 evolve the terrain and transfer sediment are often preferred in WSMs, however with simplifications that can restrict  
80 model ability to accurately replicate observed inundation extent or depositional patters. Such simplifications include  
81 omitting debris flow erosion and bulking in runout channels, limiting flow to only a single cell in the steepest  
82 downstream direction, and assuming debris flows only occupy the width of a single cell (e.g., Tucker and Bras, 1998;  
83 Istanbuluoglu and Bras, 2005) or link of a channel network (Benda and Dunne, 1997).

84 To bridge the scalable functionality of WSMs with the predictive accuracy of landslide inundation hazard models,  
85 without the computational overhead of a detailed mechanistic representation of the runout process, or difficult  
86 parameterization typical of other models, we developed a new, reduced\_–complexity landslide runout model, called  
87 MassWastingRunout (MWR). MWR models landslide runout starting from the source area of the landslide, making it  
88 easily compatible with WSMs that internally determine [the initial](#) landslide [body area-size](#) and location. MWR tracks  
89 sediment transport and topographic change downstream, and evolves the attributes of the transport material. MWR  
90 can be calibrated by adjusting just two parameters ( [\$S\_c\$  and  \$q\_c\$ , described in Section 2](#)) and is augmented with a Markov  
91 Chain Monte Carlo (MCMC) calibration utility that automatically parameterizes model behavior to observed runout  
92 characteristics (e.g., erosion, deposition, extent). MWR also includes a built-in utility called MWR Probability,  
93 designed for running an ensemble of simulations to develop probabilistic [debris flow](#)[landslide runout](#) hazard maps.

94 In this paper, we present the conceptualization and numerical implementation of the MWR model (Section 2), describe  
95 the calibration utility and its probabilistic implementation (Section 3) and demonstrate basic model response to  
96 topographic convergence and slope on a series of synthetic terrains (Section 4). Event-scale applications to replicate  
97 observed runout extent, sediment transport, and topographic change at four topographically and geologically unique  
98 field sites ([see Figure 1](#)) are discussed ([Figure 1; described in](#) Section 5). We test MWR’s predictive ability using the  
99 parameterization of one site to predict runout hazard at a nearby site and show a brief example of Monte Carlo model  
100 runs to determine runout probability from [initial landslide source areas defined by an expert-determined potentially](#)  
101 [unstable slope or](#) a hydrologically-driven landslide hazard [map-model or an expert-determined potentially unstable](#)  
102 [slope](#) (Section 6). We conclude with a short summary of MWR model performance and discuss how a calibrated  
103 MWR can be incorporated into WSMs.





104

105 **Figure 1:** Example landslides [that are](#) used to evaluate calibrated MWR performance: (a) Cascade Mountains, WA: a large debris  
 106 avalanche over steep, broadly convergent terrain (photo credit: Stephen Slaughter). (b) Black Hills, WA: large debris flows over a  
 107 broadly convergent, gently sloped valley (photo credit: Stephen Slaughter). (c) Rocky Mountains, CO: a moderate sized debris  
 108 avalanche over steep, unconfined to divergent hillslope. (d) Olympic Mountains, WA: small debris flows in steep, highly  
 109 convergent channels. [Image scale varies with depth, but approximate scale of the image is indicated at the location of the scale bar.](#)

110 **2. Description of the MassWastingRunout model**

111 **2.1 Overview of the cellular-automaton [Modelling-modelling](#) approach**

112 MWR is coded as a discrete cellular automaton (CA) model. CA models apply a set of equations or rules (deterministic  
 113 or probabilistic) to individual cells of a grid to change the numerical or categorical value of a cell state (e.g., Codd,  
 114 1968). In earth sciences, CA models are widely used to model everything from vegetation dynamics (e.g., Nudurupati  
 115 et al., 2023) to lava flows (e.g., Barca et al., 1993) to geomorphic transport, in which gravitationally directed erosion

116 and depositional processes modify a digital elevation model (DEM) representation of a landscape (e.g., Chase, 1992;  
117 Crave & Davy, 2001; Murray & Paola, 1994; Tucker et al., 2018). Existing CA-based landslide runout models include  
118 [models by](#) Guthrie and Befus (2021), D’Ambrosio et al. (2003) and Han et al. (2021). In all of these models, runout  
119 behavior is controlled by topographic slope and rules for erosion and deposition but conceptualization and  
120 implementation differ.

121 In MWR, mass\_continuity is central to model conceptualization. Of the wide range of processes described in the  
122 introduction that control observed runout, MWR explicitly represents erosion, deposition, and flow resistance due to  
123 debris size and vegetation. Material exchange between the runout material and underlying terrain as well as flow  
124 resistance determines runout extent and landscape evolution. Model rules are designed such that they can be  
125 parameterized from field measurements. Finally, in MWR, most computations occur only at the location of moving  
126 debris, in a manner analogous to the “mobile” cellular automaton implementation of Chase (1992).

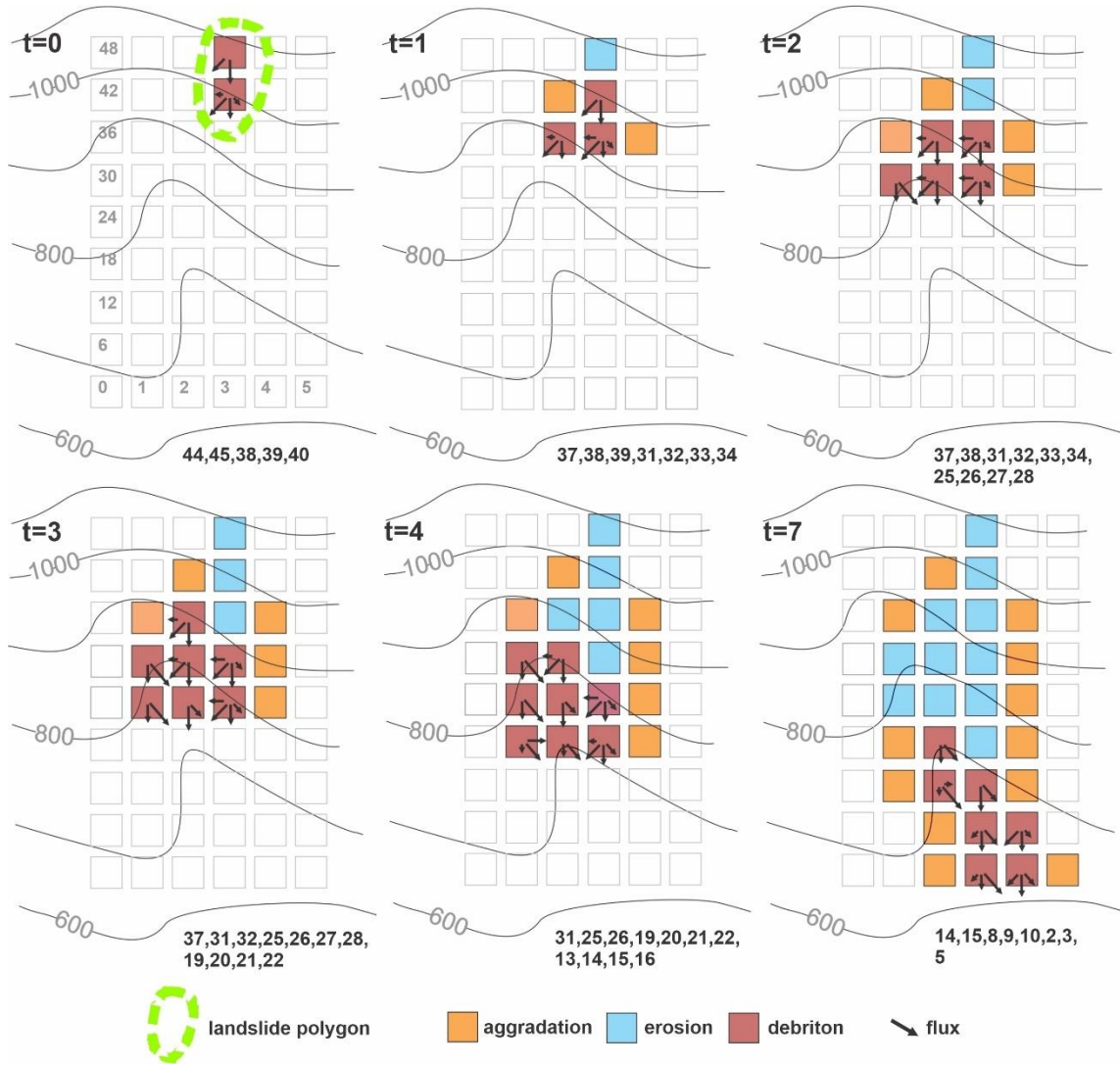
127 Chase (1992) modelled precipitation-driven surface erosion by randomly placing single packets of precipitation on a  
128 DEM, which then moved from higher elevation to lower elevation grid cells, eroding and transporting sediment as a  
129 function of the slope between the cells. The individual packets of precipitation were referred to as precipitons. In  
130 MWR, since we route the downslope progression of debris from a specified mass wasting source area, we refer to  
131 these packets of debris as “debritons”. The debritons represent debris flux, here defined as a volume of debris  
132 transferred per model iteration per grid-cell area, [ $\text{m}^3/\text{m}^2/\text{iteration}$ ] and are equivalent to the flow depth in the cell.

133 The present implementation of the MWR algorithm is coded in Python and developed as a component of the Landlab  
134 earth surface modeling toolkit (Barnhart et al., 2020; Hobbey et al., 2017). MWR uses the Landlab raster model grid,  
135 which consists of a lattice of equally sized, rectangular cells. Topographic elevation, derived topographic [attributes](#)  
136 [properties](#) like slope and curvature, and other spatially varying attributes such as regolith depth and grain size, are  
137 recorded at nodes in the center of each cell (see Figure 5 of Hobbey et al., 2017). In the subsequent sections we describe  
138 the model theory. ~~Note that a~~All the notations of parameters and variables used in ~~this the~~ theory are listed in [the](#)  
139 [Notation sectionSection 10](#).

## 140 **2.2 Mobilization of the initial mass wasting source material (Algorithm 1):**

141 To initiate MWR, the user provides maps of initial topography, regolith depth, and the location and depth of the mass  
142 wasting source material (e.g., [the initial](#) landslide body). Each raster model grid node in the mass wasting source  
143 material is designated as a debriton (Figure 2, iteration  $t = 0$ ) with a magnitude equal to the mass wasting source  
144 material depth and basal elevation equal to the initial topography minus the mass wasting source material depth. The  
145 basal elevation can be thought to represent the rupture or slip surface of the source material and the redistribution  
146 (flux) of each debriton to its downslope nodes (receiver nodes) is determined as a function of the slope of the slip  
147 surface. ~~Note that if the depth of the wasting source material is spatially variable (e.g., a rotational failure), the slope~~  
148 ~~of the slip surface will not match the slope of the initial terrain surface.~~At the lowest-elevation debriton of the source  
149 material, flux to its downslope nodes is determined using the surface slope of the initial DEM (see flow direction of  
150 lowest node in Figure 3a). This implementation helps to ensure that the lowest-elevation debriton in the mass wasting  
151 source material moves downslope and movement of upslope debritons are impacted by the geometry of the mass

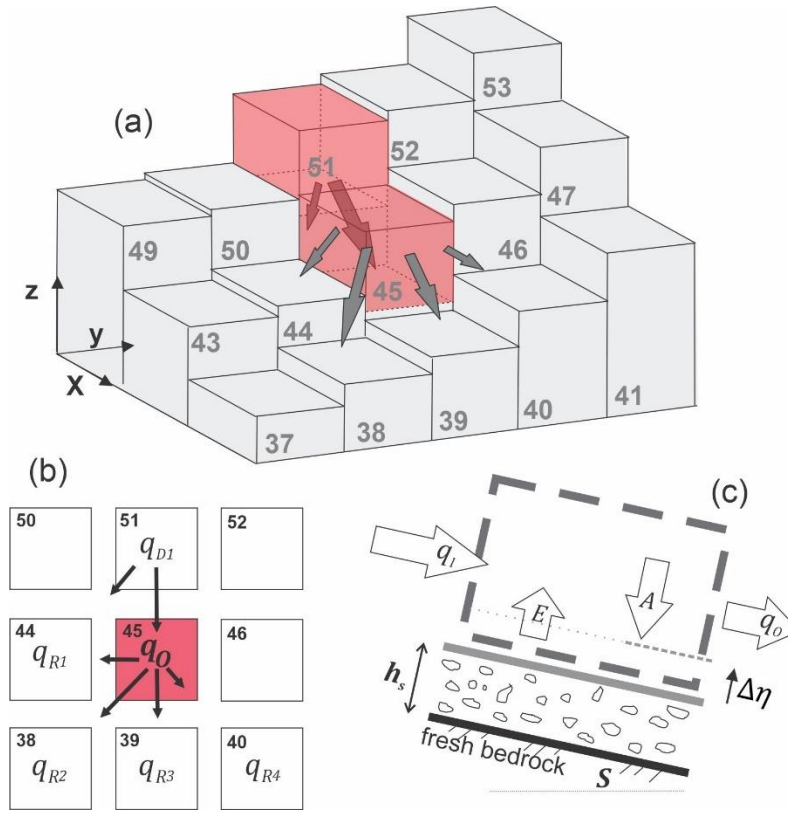
152 wasting source material. For example, the receiver nodes of the lowest-elevation debris-ton in the landslide illustrated  
 153 in Figure 2 (iteration  $t = 0$ , detailed in Figure 3a) would be identified as those among the eight neighboring nodes  
 154 whose initial topographic elevation was less than the initial topographic elevation of the node while for the debris-ton  
 155 at node 51, the receiver nodes would be identified as those among the eight neighboring nodes whose topographic  
 156 elevation is less than the topographic elevation of the terrain underlying the debris-ton (the slip surface).



157

158 **Figure 2.** Illustration of initial mass wasting release ( $t=0$ ) and runout down a steep, convergent slope. Variable  $t$  indicates model  
 159 iteration (not time). Notice how the flow elongates and widens as the model progresses and the number of receiver nodes (the list  
 160 of receiver nodes numbers listed at bottom of each panel) and quantity of mobilized material increase, changes with each iteration.  
 161 The flow elongates and widens as the number of receiver nodes increase and stops when the number of receiver nodes is zero. If  
 162 the incoming flux (sum of all incoming debris-ton) to a node is less than  $q_c$ , the material stops, causing aggradation.





163

164 **Figure 3.** (a) Three-dimensional illustration of iteration  $tt = 0$  in Figure 2, showing initial source material nodes (represented by  
 165 red cells) and flux towards downslope nodes. Except for the lowest elevation node in the mass wasting source material, all debritons  
 166 are directed downslope based on the underlying topographic slope (compare flow directions of node 51 to node 45); (b) Distribution  
 167 of  $q_o$  to downslope nodes 38, 39, 40 and 44; (c) illustration of mass continuity applied to any node that receives a debriton.

168

169 **2.3 Flow routing and rules for debris flow erosion, deposition and resistance (Algorithm 2)**

170 Algorithm 2 is essentially the runout model. It determines how each debriton traverses and modifies the landscape.  
 171 After receiver nodes from the first model iteration are determined in Algorithm 1 (iteration  $tt=0$ ), Algorithm 2 is  
 172 repeatedly implemented until all material has deposited (i.e., there are no debritons). Each debriton moves one grid  
 173 cell per model iteration, the larger the landslide size, the more iterations necessary to evacuate the landslide. As each  
 174 debriton moves, it may erode or aggrade the landscape, impacting the movement of any upslope debritons. As is  
 175 common with other reduced complexity models, we assume that inertial effects have negligible impact on flow  
 176 behavior (i.e., the kinematic flow approximation). The downslope redistribution of a debriton or flux to each of a  
 177 node's  $i$ -th receiver nodes ( $q_{R_i}$ ) is determined as a function of topographic slope (slope of terrain under the debriton)  
 178 using the Freeman (1991) multiflow-multiple flow direction algorithm:

179 
$$q_{R_i} = q_o \frac{S_i^a}{\sum_{i=1}^{Nr} S_i^a} \quad (1)$$

180 where  $q_o$  is the total out-going flux from the node and has units of depth [m] per model iteration,  $Nr$  is the number  
 181 of receiving nodes,  $i$  is the index for each receiver node (e.g.,  $i = 1, 2 \dots Nr$ ) and  $S_i$  is the underlying topographic

182 slope to the  $i$ -th receiver node (Figure 3b). The Freeman (1991) [multiple flow](#) direction algorithm is a  
 183 commonly used approximation for two-dimensional flow, and in this implementation it is handled by a pre-existing  
 184 Landlab flow-routing component. The exponent  $a$  controls how material is distributed to downslope nodes, [with](#)  
 185 [higher values causing narrower flow \(Holmgren 1994\)](#). In a braided river cellular-automaton model, Murray and Paola  
 186 (1997) used an approximation for turbulent shallow water flow to justify  $a = 0.5$  (which is the exponent on the slope  
 187 factor in channel friction laws). For our application, we found MWR provided a closer fit to observed mass wasting  
 188 runout if  $a = 1$ , suggesting that the material behavior is more similar to linear-viscous shear flow than to wall-bounded  
 189 turbulent shear flow ([e.g., as the runout debris flows downslope, it tends to spread less than shallow turbulent water](#)).  
 190 The total incoming flux (again, in units [m] per model iteration) towards a given node ( $q_I$ ), is determined by summing  
 191 the flux from each of the node's donor nodes:

$$192 \quad q_I = \sum_{j=1}^{Nd} q_{D_j} \quad (2)$$

193 Where  $Nd$  is the number of donor nodes, and  $q_{D_j}$  is the flux from node  $D_j$  (the  $j$ -th donor node,  $j = 1, 2, \dots, Nd$ ; Figure  
 194 3b).

195 As noted by Tucker and Hancock (2010), the flow depths calculated from two-dimensional flow approximations like  
 196 (1) can be influenced by the grid-size used to represent the terrain and depending on [terrain slope and convergence, the](#)  
 197 [boundary conditions,](#)—neglection of pressure and momentum forces may lead the model to underestimate or  
 198 overestimate flow width in some circumstances. Rengers et al. (2016) noted that this same issue occurs when using a  
 199 kinematic wave approximation of the shallow water equations because the kinematic wave approximation lacks a  
 200 pressure term that would normally allow the modelled water surface to spread out. [We consider flow depths](#)  
 201 [determined from \(2\) as meaningful in the sense that they vary as a function of flux but less meaningful in the sense](#)  
 202 [that they are affected by the limitations noted above. Furthermore, For](#) for the purpose of determining flow-depth-  
 203 dependent erosion rates described later in this paper, and to provide a simplified representation of the effect of pressure  
 204 forces, we constrain flow depths to no more than a maximum flow as:

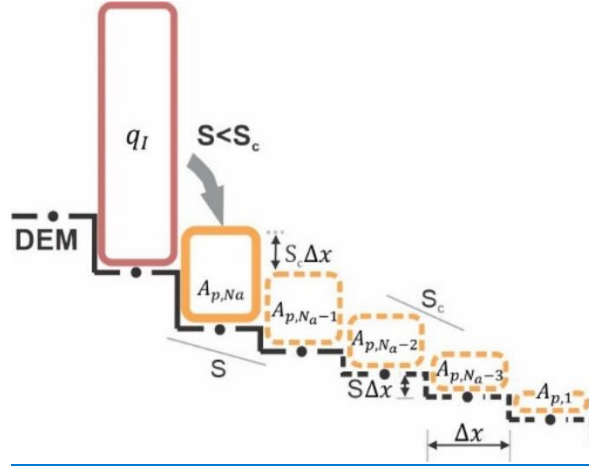
$$205 \quad h = \min(h_{max}, q_I) \quad (3)$$

206 Where  $h_{max}$  is an effective upper limit to flow depth, that in practice can be approximated as the maximum observed  
 207 flow depth, as inferred from field indicators or assigned based on expert judgement (See Section 5) and  $h$  is the  
 208 corrected flow depth used to calculate flow shear stress. This correction allows erosion rates to vary with flux but  
 209 prevents unreasonably large values. This flow depth correction does not violate the conservation of mass and runout  
 210 mass balance, as  $h$  is only used to calculate flow shear stress.

211 To determine aggradation ( $A$ ) at a node, we use a critical slope ( $S_c$ ) constraint that permits computationally-rapid  
 212 distribution of  $q_I$  over multiple nodes. Critical slope constraints or rules are common to many reduced-complexity  
 213 and landscape evolution models. Chen et al. (2023) showed that when flow inertia can be ignored,  $S_c$  can be  
 214 approximated from the surface slope of observed deposits. Several landscape evolution models use a  $S_c$ -based  
 215 nonlinear, nonlocal aggradation scheme (e.g., Campforts et al., 2020; Carretier et al., 2016) but when this rule is  
 216 implemented with the debriton framework described above, unreasonably tall deposits result when  $q_I$  is large and



217 slope at the node ( $S \ll S_c$ ). To resolve this problem, aggradation depth can be limited to  $A \leq S_c \Delta x$ , (where  $\Delta x$  grid  
 218 cell length), but we found that this constraint results in long deposits that parallel the underlying slope when  $q_I$  is  
 219 large. Instead, MWR computes the aggradation depth at a node assuming that the aggradation will spread over  $N_a$   
 220 nodes until all of  $q_I$  is deposited and that the surface slope of the overall deposit will be equal to  $S_c$ , as shown in Figure  
 221 4 and described as follows.



222  
 223 **Figure 4.** Illustration of aggradation rule used in MWR when  $q_I$  is assumed to spread over 5 nodes ( $N_a = 5$ ). Solid  
 224 yellow box indicates deposition aggradation at node  $n$  amount at a given node. Dashed yellow boxes and lines  
 225 indicate the hypothetical geometry of assumed the aggradation beyond the node deposition and underlying  
 226 topography. Dots along DEM surface are nodes.

227 Aggradation at a node is determined as:

$$228 \quad A = \begin{cases} 0, & S \geq S_c \\ \min(A_{p,N_a}, q_I), & S < S_c \end{cases} \quad (4)$$

229 Where  $S$  is the steepest slope to the node's eight neighbouring nodes,  $A_{p,N_a}$  is a potential aggradation depth ( $A_p$ )  
 230 necessary to form a deposit that: (1) begins at the node and spreads over  $N_a$  consecutive nodes; (2) has a total volume  
 231 equal to  $q_I \Delta x^2$ ; (3) a surface slope equal the critical slope  $S_c$  and; (4) an underlying topographic slope equal to the  
 232 steepest slope at the node and assumed constant over the  $N_a$  consecutive nodes of deposition ( $S_n$ ). From this assumed  
 233 deposit, we can analytically define  $A_{p,N_a}$  and  $N_a$  as a function of  $q_I$ ,  $S_c$  and  $S_n$  as follows:

234 First,  $q_I$ , calculated from (2), can be used to calculate  $A_{p,i}$  by expressing  $q_I$  as the sum of the  $N_a$  deposits that make  
 235 up the overall deposit as:

$$236 \quad q_I = \sum_{i=1}^{N_a} A_{p,i} \quad (5)$$

237 where  $A_{p,i}$  is the  $i$ -th deposition amount in the deposit and  $i = 1$  is the last node of deposition ( $A_{p,1}$ ; see Figure 4).  
 238 Since we assume the deposit slope and underlying topographic slope are uniform, the deposition amount at any of the  
 239  $N_a$  nodes can be determined from  $A_{p,1}$  as:

$$240 \quad A_{p,i} = A_{p,1} + (i - 1)\Delta x(S_c - S_n) \quad (6)$$

241 From (6) we can re-write (5) as a function of  $A_{p,1}$  and rearrange to define  $A_{p,1}$  as a function of  $q_I$ :

$$242 \quad A_{p,1} = \frac{1}{N_a} q_I - \frac{N_a - 1}{2} \Delta x (S_c - \frac{S_c}{N_a}) \quad (7)$$

243 Substituting (7) into (6) and solving for  $i = N_a$ , we get an expression for  $A_{p,N_a}$ :

$$244 \quad A_{p,N_a} = \frac{1}{N_a} q_I + \frac{N_a - 1}{2} \Delta x (S_c - \frac{S_c}{N_a}) \quad (8)$$

245 Equation (8) can be rearranged into a quadratic equation and solved for  $N_a$  as:

$$246 \quad N_a = \frac{-A_{p,1} + \frac{1}{2} \Delta x (S_c - \frac{S_c}{N_a}) \pm \sqrt{\left( A_{p,1} - \frac{1}{2} \Delta x (S_c - \frac{S_c}{N_a}) \right)^2 + 2 \Delta x (S_c - \frac{S_c}{N_a}) q_I}}{\Delta x (S_c - \frac{S_c}{N_a})} \quad (9)$$

247 We use (8) to solve for  $A_{p,N_a}$  and (9) to solve for  $N_a$  assuming  $A_{p,1} = 1/2 \Delta x S_c$  and rounding the positive solution to  
 248 the nearest integer. When implemented using a single debriton, released on a two-dimensional hillslope as illustrated  
 249 in Figure 4, the debriton deposits over  $N_a$  nodes at a uniform slope equal to  $S_c$ . When implemented on an actual three-  
 250 dimensional terrain, the interaction between multiple debritons in multiple directions creates a complex deposit whose  
 251 slope changes with  $S_c$ .

252 To determine erosion depth ( $E$ ) [m/iteration], we constrain  $E$  to the lesser of a potential erosion depth,  $h_e$ , and local  
 253 regolith depth,  $h_r$ :

$$254 \quad E = \min (h_r, h_e) \quad (10)$$

255 where  $h_e$  is computed as a function of the basal shear stress of the flow,  $\tau$  [Pa], (Equations 12 and 13) and the critical  
 256 shear stress ( $\tau_c$ ) of the regolith at the node [Pa]:

$$257 \quad h_e = k(\tau - \tau_c)^f \quad (11)$$

258 The coefficient  $k$  is an erodibility parameter [m/Pa<sup>f</sup>]. Stock and Dietrich (2006) showed that  $k$  encapsulates substrate  
 259 properties. If  $h_e$  is used to represent erosion over geomorphic time scales, with repeated debris flow occurrences in a  
 260 single model iteration,  $k$  becomes associated with debris flow length and frequency (Perron, 2017). In our application  
 261 since we are modelling the erosion associated with a single runout event, as represented by the downslope movement  
 262 of the debritons, the coefficient  $k$  therefore needs to scale  $h_e$  on the order of the average erosion depth caused by a  
 263 single debriton. Using this logic,  $k$  can be computed using the observed average erosion depth and an estimated length  
 264 of the runout material that caused the erosion. Further details on how we determine  $k$  from observed runout are  
 265 included in the [Supplementary Material Appendix](#). The exponent  $f$  controls the non-linearity of  $h_e$  [with shear stress](#).  
 266 Many authors (Chen & Zhang, 2015; Frank et al., 2015; Shen et al., 2020) use a value of 1 for  $f$  but field measurements  
 267 by Schürch et al. (2011) (see their Figure 3) suggest that  $f$  may be less than 1 if  $\tau$  is assumed to vary linearly with  
 268 flow depth, particularly at flow depths greater than 3 meters.

269 MWR includes two options for defining  $\tau$ : (1) a quasi-static basal shear stress approximation or (2) a grain-size-based  
 270 shear stress approximation. The quasi-static basal shear stress approximation (e.g., Takahashi, 2014) is defined as:

$$271 \quad \tau = \rho g h \sin \theta \quad (12)$$

272 where  $\rho$  is the density of mass wasting material (grain and water mixture) [kg/m<sup>3</sup>],  $g$  is gravity [m/s<sup>2</sup>]-and,  $h$  is the  
 273 adjusted flow depth described in (3) and  $\theta$  is the topographic slope ( $\tan^{-1}(S)$ ) measured in degrees.

274 The grain-size-based shear stress approximation is defined using an empirical formula by Bagnold (1954):

$$275 \quad \tau = \sigma \tan \varphi \quad (13)$$

276 Where  $\sigma$  is normal stress [Pa],  $\varphi$  is the collision angle between grains, measured from the vertical axis (See Bagnold,  
 277 1954), with a value of  $\tan \varphi$  typically equal to 0.32. Stock and Dietrich (2006) defined  $\sigma$  as:

$$278 \quad \sigma = \cos \theta v_s \rho_s D_s^2 \left( \frac{du}{dz} \right)^2 \quad (14)$$

279 Where  $v_s$  is the volumetric solids concentration,  $\rho_s$  is density of the solids [kg/m<sup>3</sup>],  $u$  is flow velocity [m/s],  $z$  is depth  
 280 below the flow surface [m],  $du/dz$  is the shear strain rate [1/s] and  $D_s$  is the representative grain size [m]. Stock and  
 281 Dietrich (2006) suggested that  $D_s$  corresponds to a small percentile of the coarsest fraction of the runout material ( $D_{88}$   
 282 to  $D_{96}$ ) and they approximated  $du/dz$  as:

$$283 \quad \frac{du}{dz} = \frac{u}{h} \quad (15)$$

284 Solely for the purpose of computing  $du/dz$ , we approximate velocity at a node using a grain-size dependent empirical  
 285 formula for debris flow velocity by Julien and Paris (2010) as:

$$286 \quad u = 5.75 u^* \log \left( \frac{h}{D_s} \right) \quad (16)$$

287 Where  $u^*$  is shear velocity ( $\sqrt{gh \tan \theta}$ ). Substituting (16), (15), (14) and (13) into (11) yields a grain-size dependent  
 288 approximation for  $h_e$  that mimics the non-linear erosion response to flow depth in Schürch et al. (2011). Additionally,  
 289 this form of  $\tau$  is advantageous because it permits landslide-driven erosion rates to scale with landslide grain size,  
 290 which can vary by lithologic region (e.g., Roda-Boluda et al. 2018). As will be shown in Section 5, we obtained  
 291 reasonable model calibration at multiple sites by defining  $D_s$  from the coarser grain sizes observed in the field at  
 292 existing runout-deposits, road-cuts and tree-throw pits.

293 Once  $A$  [m] and  $E$  [m] have been determined, total out-going flux per iteration,  $q_o$  [m] is determined as (see Figure  
 294 3c):

$$295 \quad q_o = \begin{cases} q_l - A + E, & q_l \geq q_c \\ 0, & q_l < q_c \end{cases} \quad (17)$$

296 Where  $q_c$  is a threshold flux for deposition. When  $q_l < q_c$ ,  $q_l$  deposits and  $q_o$  becomes zero. The threshold flux  $q_c$   
 297 conceptually represents the flow depth below which flow resistance is large enough to cease the forward momentum  
 298 of the flow, whether in the form of internal friction or friction due to vegetation and obstructions (e.g., large clasts or  
 299 logs). The density and water content of  $q_l$ ,  $A$ , and  $E$  are treated as uniform and surface runoff, such as channelized  
 300 stream flow or hillslope-infiltration-excess runoff, that might mix with  $q_l$ .  $A$ , or  $E$  is ignored. Once  $q_l$ ,  $A$ ,  $q_o$  and  $E$   
 301 have been determined, change in elevation at a node ( $\Delta\eta$ ) is calculated as:

$$302 \quad \Delta\eta = A - E \quad (18)$$

303 Attributes (e.g., grain size, organic content or any other attribute that is transferred in the flow) of the debriton and  
 304 regolith are updated using a volumetric-weighted average approach. First, for each regolith attribute being tracked by  
 305 the model (e.g., grain size), the attribute value delivered to a node from its donor nodes ( $\xi_D$ ) is determined as:

$$306 \quad \xi_D = \frac{\xi_D \cdot q_D}{q_I} \quad (19)$$

307 where  $q_D$  is a vector containing all  $q_{D_j}$  sent to the node,  $\xi_D$  is a vector containing the incoming attribute values for  
 308 each  $q_{D_j}$ , and  $q_I$  is the sum of incoming flux from donor nodes defined by (2).

309 Second, the attribute value sent from a node to its receiver nodes ( $\xi_R$ ) is determined as:

$$310 \quad \xi_R = \frac{\xi_{t-1} E + \xi_D (q_I - A)}{q_O} \quad (20)$$

311 where  $\xi_{t-1}$  is the attribute value at the node before any aggradation (i.e., the previous iteration attribute value). Finally,  
 312 the attribute value at the node, updated to account for erosion and aggradation ( $\xi$ ) is:

$$313 \quad \xi = \frac{\xi_{t-1} (h_r - E) + \xi_D A}{A + h_r - E} \quad (21)$$

314 Regolith thickness ( $h_r$ ) and topographic elevation ( $\eta$ ) are updated at a node as:

$$315 \quad \eta = \eta_{t-1} + \Delta\eta \quad (22)$$

$$316 \quad h_r = h_{r,t-1} + \Delta\eta \quad (23)$$

317 Where  $\eta_{t-1}$  and  $h_{r,t-1}$  are the topographic surface elevation and regolith thickness at the node from the previous  
 318 model iteration. After regolith thickness and topographic elevation have been updated for each debriton, the multi-  
 319 direction slope of the DEM, which is used for routing the debritons in the next model iteration, is recomputed from  
 320 the topographic surface.

321 Using the above approach, debritons may become obstructed if they encounter a topographic pit or flat topography in  
 322 the DEM. To allow a debriton to pass an obstruction, we rely on a simple work-around: upon encountering the  
 323 obstruction, the debriton is directed to itself and some portion of the debris is deposited based on (4). At the end of  
 324 the model iteration, the node elevation and slope are updated. During the next iteration, if the remaining mobile debris  
 325 is no longer obstructed, it moves to its downslope node(s). If the node is still obstructed, it is again sent to itself until  
 326 either all material has deposited or the elevation of the node exceeds that of its neighbour nodes, allowing the debriton  
 327 to move downslope.

### 328 3. Calibration and MWR probability

#### 329 3.1 Calibration utility

330 MWR includes an adaptive Markov Chain Monte Carlo (MCMC) calibration algorithm described by Coz et al. (2014)  
 331 and Renard et al. (2006). [The MCMC algorithm is implemented as a utility for MWR and identifies a single set of](#)  
 332 [parameters that best match MWR output to an observed landslide runout dataset. The observed runout dataset can](#)  
 333 [consist of a single or multiple landslides. Depending on user input, MWR simultaneously or sequentially models](#)



334 [runout from each landslide source area in one model run. To use the calibration utility](#), ~~The~~ the user provides an initial  
 335 (prior) guess of the parameter values and their respective probability distribution functions (PDF) that calibrate the  
 336 ~~model-MWR~~ to a specific site. Then, the calibration ~~algorithm-utility~~ randomly selects a set of [trial](#) parameter values  
 337 ( $\Lambda$ ) from the prior PDFs and runs MWR using  $\Lambda$ . Once the model has completed the run, the algorithm evaluates the  
 338 posterior likelihood of the parameter set ( $L(\Lambda)$ ) as a lumped index of model ability to replicate observed runout  
 339 (described below) and the prior likelihood of the parameter set. After the first  $L(\Lambda)$  has been determined, the ~~algorithm~~  
 340 ~~utility~~ selects a new set of parameters ( $\Lambda_{t+1}$ ) by jumping some distance [\(described below\)](#) from each parameter in  $\Lambda$   
 341 space. Depending on the value of  $L(\Lambda_{t+1})$ , the algorithm either stays at  $\Lambda$  or moves to  $\Lambda_{t+1}$ . This Markov process is  
 342 repeated a user-specified  ~~$N$~~  [number of](#) times. Jump direction is random, but the algorithm is adaptive because the  
 343 jump distance changes depending on ~~how often~~ [if  \$L\(\Lambda\_{t+1}\) > L\(\Lambda\)\$  occurs more than a user specified threshold value](#).  
 344 For a detailed description of the algorithm see Coz et al. (2014).

345 The  $L(\Lambda)$  index is estimated as the product of the prior probability of the selected parameter values,  $p(\Lambda)$ , and three  
 346 other performance metrics as:

$$347 \quad L(\Lambda) = p(\Lambda) * \Omega_T * \frac{1}{\Delta\eta_E^2} * \frac{1}{Q_{sE}^2} \quad (24)$$

348 where  $\Omega_T$  is the Lee-Salle index (Heiser et al., 2017) for [evaluating](#) model planimetric fit; and  $\Delta\eta_E$  and  $Q_{sE}$  are new  
 349 dimensionless indices, proposed for this study [\(described below\)](#). The indice  $\Delta\eta_E$  is the volumetric error of the  
 350 modelled topographic change [over the entire model domain](#) normalized by the observed total mobilized volume (initial  
 351 landslide [body](#) + erosion volume). The indice  $Q_{sE}$  is the mean-cumulative ~~sediment export flow~~ error along the  
 352 modelled runout path normalized by the observed mean cumulative flow. Larger values of  $\Omega_T$  and smaller values of  
 353  $\Delta\eta_E$  and  $Q_{sE}$  indicate modelled runout more closely fits observed. Note that we add a value of 1 to  $\Omega_T$  and use the  
 354 squared-~~reciprocal~~ values of  $\Delta\eta_E$  and  $Q_{sE}$  in (24) so that the magnitude of  $L(\Lambda)$  is always equal to or greater than  
 355 zero and increases with improved fit. The metric  $\Omega_T$  is written as:

$$356 \quad \Omega_T = \frac{\alpha - \beta - \gamma}{\alpha + \beta + \gamma} + 1 \quad (25)$$

357 where  $\alpha, \beta$  and  $\gamma$  are the areas of matching, overestimated and underestimated runout extent, respectively.

358 The spatial index for volumetric error,  $\Delta\eta_E$ , is determined as:

$$359 \quad \Delta\eta_E = \sqrt{\frac{\sum_{i=0}^p [(\Delta\eta_{oi} - \Delta\eta_{mi})\Delta x^2]^2}{V^2}}. \quad (26)$$

360 Where  $V$  is observed total mobilized volume and  $p$  is the number of nodes in [the area made up of the matching,](#)  
 361 [overestimated and underestimated areas of runout extent](#)~~the modelled runout extent~~, and  $\Delta\eta_{mi}$  and  $\Delta\eta_{oi}$  are the  
 362 modelled and observed topographic change [m] at the  $i$ -th node [within that extent](#)~~within the runout extent~~.

363 To calculate  $Q_{sE}$ , we first determine the cumulative ~~debris export~~ (flow) volume ( $Q_s$ ) at each node,  $j$ , ~~( $Q_{sj}$ )~~ along the  
 364 runout profile, in a manner similar to the flow volume/mass balance curves in Fannin and Wise (2001) and Hungr and  
 365 Evans (2004):

366  $Q_{s-j} = -\Delta x^2 \sum_{i=1}^{u_j} \Delta \eta_{i,j}$  (28)

367 where  $\Delta \eta_{ij}$  is the topographic change [m] at the  $i$ -th node located upstream of node  $j$ , and  $u_j$  is the total number of all  
 368 nodes located upstream of  $j$ .  $Q_{s-j}$  is computed for both the observed and modelled runout [path](#) ( $Q_{sO-j}$  and  $Q_{sM-j}$   
 369 respectively) and  $Q_{sE}$  of a runout is determined as:

370  $Q_{sE} = \sqrt{\frac{\frac{1}{r} \sum_{j=1}^r (Q_{sO-j} - Q_{sM-j})^2}{Q_{sO}^2}}$  (29)

371 Where  $r$  is the number of nodes along the [center line of the runout profilepath](#), and  $\overline{Q_{sO}}$  is the observed mean  
 372 cumulative flow.

373 As will be detailed in Section 5, field estimates for  $S_c$  and  $q_c$ , vary over the length of the runout path. To account for  
 374 the heterogeneity of  $S_c$  and  $q_c$ , we estimate prior distributions of potential  $S_c$  and  $q_c$  values from field/remote sensing  
 375 measurements. Then, from model calibration to a DEM-of-Difference (pre-runout DEM subtracted from the post-  
 376 runout DEM; DoD) using the calibration utility, we find single values of  $S_c$  and  $q_c$  that allow the modelled DoD to  
 377 replicate the observed DoD .

378 We run the calibration utility using a single Markov chain of 2000 repetitions. At most sites, the model converged  
 379 relatively quickly on a solution and we therefore didn't consider burn-in or evaluate convergence (e.g., Gelman et al.  
 380 2021) [and considered 2000 repetitions adequate](#). Future implementations of the calibration utility may include multiple  
 381 chains, burn-in and a check for convergence. As a final note, many debris flow runout models are evaluated using  $\Omega_T$   
 382 or variations of  $\Omega_T$  alone (e.g, Gorr et al., 2022; Han et al., 2017) and the MWR calibration utility can also be run  
 383 solely as a function of  $\Omega_T$ . However, we found that calibration based on  $\Omega_T$  (*i.e.*, [runout extent](#)) alone results in high  
 384 parameter equifinality (e.g., Beven 2006); multiple parameter sets result in an equally calibrated model as evaluated  
 385 by  $\Omega_T$ . As such, we recommend calibrating debris flow/[landslide runout](#) models to an observed DoD. If [repeated](#) lidar  
 386 is available, a DoD can be obtained from before and after scans of the observed runout event. Alternatively, a DoD  
 387 can be created by hiking the observed runout event and mapping field-interpreted erosion and deposition depths.  
 388 Additional details on how we prepared DoDs for multiple sites are included in the Supplementary Material.

389

390 **3.2 Mapping landslide runout hazard**

391 MWR includes an additional utility called MWR Probability that produces landslide runout probability maps. MWR  
 392 Probability repeatedly runs MWR a user specified  $N_p$  times, each repetition with a different, randomly sampled  
 393 parameter set from the posterior parameter PDFs produced by the calibration utility. MWR Probability includes three  
 394 options for specifying the initial mass wasting source material: (1) a user-provided landslide source area polygon(s)  
 395 based on field and/or remote sensing observations; (2) a user-defined hillslope susceptible to landslides (e.g.,  
 396 potentially unstable slope), where landslide area and location are randomly selected within, but no larger than the  
 397 hillslope; this option is useful when the extent of a potential landslide is unknown; and (3) a series of mapped landslide  
 398 source areas within a watershed, as determined by an externally run Monte Carlo landslide initiation model (e.g.,

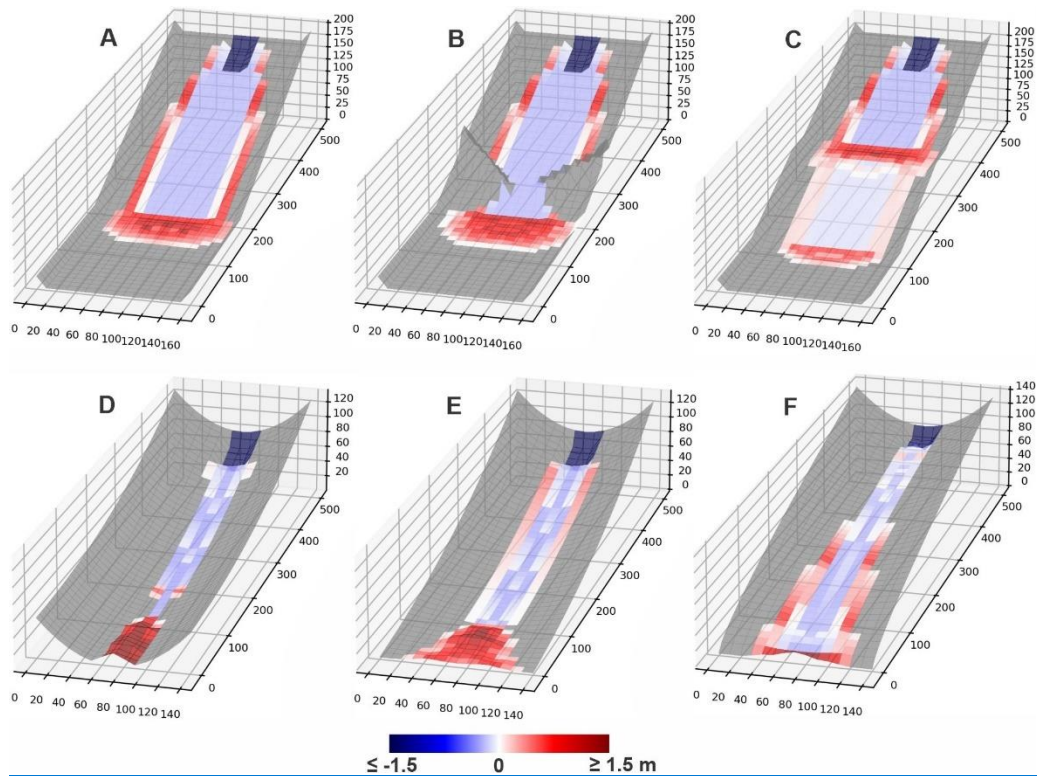
399 Hammond et al. 1992; Strauch et al., 2018) ; this option is useful for regional runout hazard applications. If using  
 400 Option 1, modelled runout probability represents uncertainty in MWR parameterization. If using Option 2 or 3,  
 401 modelled runout probability reflects uncertainty in both MWR parameterization and landslide location and size.  
 402 For all three run options, each model iteration begins with the same initial topography. After  $Np$  model simulations,  
 403  $Np$  different versions of the post-runout landscape are created, ~~and model performance for each are evaluated. After~~  
 404  ~~$Np$  model runs and,~~ probability of runout at each ~~model~~-node is determined as:

$$405 \quad P(\Delta\eta) = \frac{\text{number}_{\sigma_f}\#(|\Delta\eta|>0)}{Np} \quad (30)$$

406 where  ~~$\text{number}_{\sigma_f}\#(|\Delta\eta| > 0)$~~  is the number of times topographic elevation at a node changes as a result of erosion or  
 407 deposition from the  $Np$  model runs. Probability of erosion or aggradation can be determined by replacing the  
 408 numerator in (30) with  ~~$\text{number}_{\sigma_f}\#(\Delta\eta < 0)$~~  or  ~~$\text{number}_{\sigma_f}\#(\Delta\eta > 0)$~~  respectively.

#### 409 **4. Basic model behavior**

410 We evaluate basic model behavior using a series of virtual experiments. The virtual experiments consist of six  
 411 synthetic terrains including: (A) a planar slope that intersects a gently sloped plane ( $S = 0.001$ ), (B) a planer slope  
 412 with a constriction, that intersects a gently-sloped plane, (C) a planar slope that has a bench mid-slope and then  
 413 intersects a gently-sloped plane; (D) a concave up, uniform-convergence slope; (E) a concave up, variable-  
 414 convergence slope that widens (convergence decreases) in the downslope direction; (F) a convex up, variable-  
 415 convergence slope that widens (convergence decreases) in the downslope direction. On each terrain, a 30-meter wide,  
 416 50-meter long and 3-meter deep landslide is released from the top of the terrain. All six terrains are covered by a 1-  
 417 meter thick regolith and use the same parameter values ( $S_c = 0.03$ ,  $q_c = 0.2$  m,  $k = 0.01$ ,  $D_{ps} = 0.2$  m). Each terrain  
 418 is represented using a 10-m grid. Experiment results are shown in Figure 5.



419

420 **Figure 5.** Shaded, 3-D visualizations of model response to six different synthetic terrains, colored according to the  
 421 DoD of the final runout surface. Shading is to scale. Red indicates a positive change in the elevation of the terrain  
 422 (aggradation) and blue indicates a negative change (erosion). Grid size is 10 meters. The 3-D representation  
 423 visualization of the DoD is exaggerated by a factor of 5 to make visible in figure. Grid size is 10 meters.

424 On Terrain A, the landslide spread as it moved downslope and formed levees along the edge of the runout path. The  
 425 width of the spread was a function of the multiple flow ~~multiflow~~ direction algorithm and resistance along lateral  
 426 margins of the runout as represented by  $q_c$ . At the slope break at the base of the slope, the material deposited at an  
 427 angle controlled by  $S_c$ . On Terrain B, the flow initially eroded and deposited identical to the first but near the slope  
 428 break, the topographic constriction forced flow depth to increase and exceed  $q_c$ , minimizing the formation of levees  
 429 (because  $q_0 > q_c$ ) and resulted in a slightly larger deposit at the base of the slope. On Terrain C, landslide runout was  
 430 again initially identical to the runout on Terrain A; however, upon intersecting the mid-slope bench, most of the runout  
 431 material deposited. A small, thinner portion did continue past the bench but eroded at a lower rate than the initial slide  
 432 upslope of the bench. Upon intersecting the flat surface at the base of the hillslope, the runout material deposited.

433 On Terrain D, the landslide and its runout were confined to the center of convergent terrain and only deposited once  
 434 the slope was less than  $S_c$ . The slide never widened because the uniformly convergent channel shape prevented  
 435 spreading and the narrower flow width maintained a higher flow depth, which prevented the formation of levees. On  
 436 Terrain E, the landslide again deposited once slope was less than  $S_c$  but because topographic convergence of Terrain  
 437 E decreases in the downslope direction, as the runout material moved downslope, the deposit spread more than on  
 438 Terrain D, which caused thinner flow and deposition along margins of the runout path. On the final terrain, Terrain F,



439 slope is always greater than  $S_c$  so deposition was limited to levees along the edge of the flow that formed as the runout  
440 spread in response to decreasing convergence.

441 MWR model behavior can be summarized as follows. The displacement and deposition of landslide material predicted  
442 by MWR responds to topography in a reasonable manner: Flow width increases as convergence decreases (e.g, Terrain  
443 F), which in turn reduces flow depth. Lower flow depths cause lower erosion rates and reduce aggradation extent.  
444 Conversely, modelled flow depth increases when convergence increases (e.g., Terrain B). Where the flow encounters  
445 broadly convergent or planer slopes, lateral levee deposits form, a common feature of landslides reported in the  
446 literature and at sites reported here (see Section 5) that detailed mechanistic models can struggle to reproduce (e.g.,  
447 Barnhart et al, 2021).

448 We did not attempt to compare MWR modelled flow with the output of shallow-water-equation based models or  
449 observed granular flows (e.g., Medina et al, 2008; McDougall and Hungr, 2004; Iverson and Denlinger, 2001; Han  
450 et al., 2015). The cellular automaton representation in MWR does not model the time-dependent evolution of debris  
451 flow velocity and depth, and conceptually moves debris instantaneously at each iteration, as driven by changes in the  
452 evolving topographic elevation field. Because of that, only the final outcome ([modelled runout extent, sediment  
453 transport and topographic change](#)) of MWR can be compared with other models or observed runout, which we do in  
454 the next section. [Also, as described in Section 2.3, behaviour of the multiple flow direction algorithm does vary with  
455 grid size. Using a coarser or finer grid, without adjusting model parametrization, could potentially change how wide  
456 the landslide spreads.](#)

## 457 **5. Model Validation:**

### 458 **5.1 Overview**

459 In this section, we demonstrate the ability of a calibrated MWR to replicate observed runout extent, sediment transport  
460 and topographic change at field sites located in the western USA and summarize model calibration results with an  
461 evaluation of MWR calibration relative to terrain attributes of the observed runout paths. Note that simply calibrating  
462 a model to match field data does not constitute a satisfactory test of model predictive ability (Iverson, 2003). Strategic  
463 testing, which involves calibrating the model to one site or period of time and then running the calibrated model at a  
464 separate site or period of time (Murray, 2013), is a better indicator. Two of our validation sites, the Cascade Mountain  
465 and Olympic Mountain sites, include two separate landslides and subsequent runout and we test model predictive  
466 ability at these sites in Section 6.

467 Calibrated model performance is demonstrated at the following field sites (see Figure 6a for locations and observed  
468 runout extent): (1) two runout events over the same hillslope in the Cascade Mountains (Washington state [WA],  
469 USA): a large debris avalanche in 2009 (Cascade Mountains, 2009) and a moderately-sized debris flow in 2022  
470 (Cascade Mountains, 2022) that inundated and flowed within a first-to-second order channel until perpendicularly  
471 intersecting a narrow river valley several hundred meters below the landslide (Figure 1a); (2) debris flows in the Black  
472 Hills (WA) sourced from a small failure along the toe of a deep-seated landslide (Black Hills, South) and a moderately-  
473 sized debris avalanche from a large road fill (Black Hills, North) that flowed several kilometers along a relatively

474 wide, broadly convergent channel before stopping (Figure 1b); (3) a single, moderately-sized debris avalanche in the  
 475 Rocky Mountains (Rocky Mountains), the majority of which flowed several hundred meters over a broadly convergent  
 476 to divergent hillslope in Colorado (Figure 1c); and (4) a 30-year chronology of small landslides and subsequent debris  
 477 flows in the Olympic Mountains (WA) in steep, highly convergent channels that flowed well over a kilometer and  
 478 coalesced into a single runout deposit in a dendritic, channelized watershed (Olympic Mountains; Figure 1d). All  
 479 landslides initiated during heavy rainfall or rain-plus-snowmelt storm events (WRCC, 2022; NRCS, 2022; Table 1)  
 480 but their runout varied in terms of erosion rate, grain size (Figure 6b), depositional behavior (Figure 6c) and the  
 481 topographic convergence of the underlying terrain.

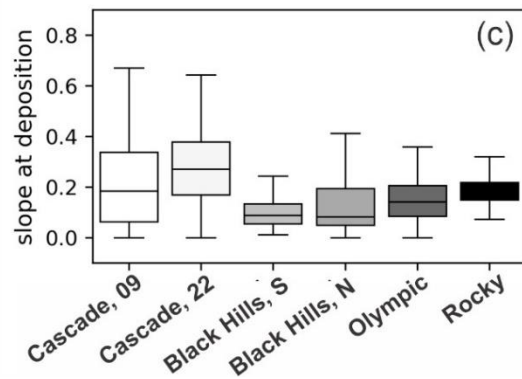
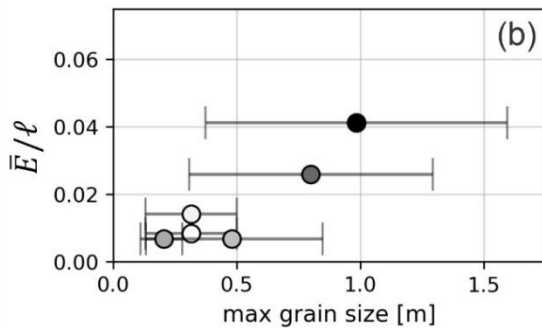
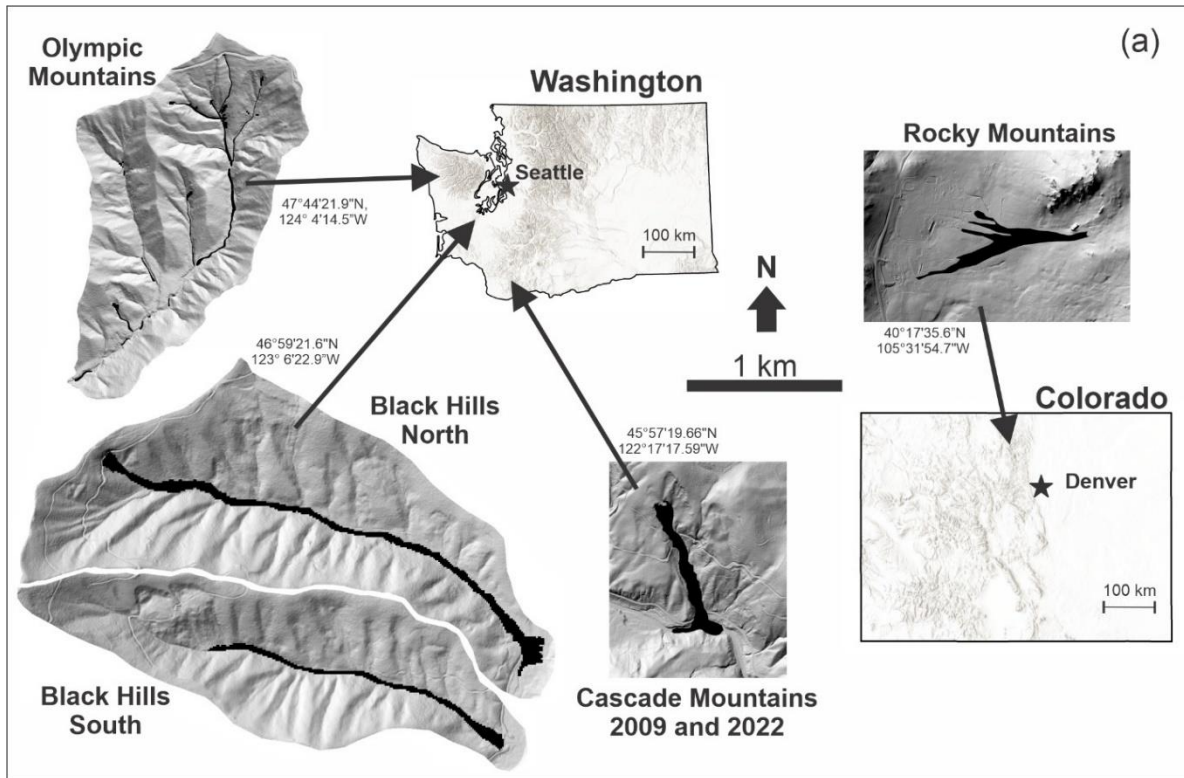
482 **Table 1.** Landslide and runout characteristics

site	Cascade Mountai ns, 09	Cascade Mountains, 22	Black Hills, south	Black Hills, north	Rocky Mountains	Olympic Mountains
<u>initial landslide body</u> length, $\ell$ [m]	185	55	80	75	40	45
<u>initial landslide body</u> width [m]	80	50	15	65	35	15
<u>initial landslide body</u> volume [m <sup>3</sup> ]	110,000	22,000	1,500	18,500	4,600	400 - 2,200
2-day cumulative precipitation + snowmelt [mm]	120+85	140+75	205+50	205+50	193+0	100 - 220 + ?
maximum grain size [m]	0.316	0.316	0.48	0.206	0.984	0.8
<u>Slope-slope</u> range of positive-net deposition [%]	1 - 15	1 - 15	<1 - 10	<1 - 8	16 - 25	5 - 15
average flow depth in scour zone [m] <sup>a</sup>	4	2	2	3	3	3
average channel slope in scour zone [m/m]	0.25	0.25	0.15	0.15	0.4	0.3
average channel width in scour zone [m]	45	20	25	35	55	10
length of erosion, [m]	600	340	1210	1345	360	2550
erosion area, $A$ [m <sup>2</sup> ]	28,400	6,600	22,800	52,400	20,800	28,900
erosion volume, $\sum E\Delta x^2$ [m <sup>3</sup> ] <sup>b</sup>	44,547	5,125	12,332	26,815	34,275	33,725
average erosion per unit length of <u>landslide</u> <u>runout debris</u> , $\bar{E}/\ell$ , [m/m]	0.0085	0.014	0.0068	0.0068	0.041	0.026
$k$	0.020	0.034	0.017	0.020	0.076	0.051
growth factor, [m <sup>3</sup> /m]	74.2	15.1	10.2	19.9	95.2	13.2
average observed $ \Delta\eta $ [m]	2.4	2.2	0.53	0.63	0.89	1.4
total erosion volume / total mobilized volume <sup>c</sup>	0.29	0.19	0.89	0.59	0.88	0.97

483 <sup>a</sup> rough approximation based on landslide volume, channel width and height of scour marks in erosion zone

484 <sup>b</sup> excludes landslide volume

485 <sup>c</sup> total mobilized volume = erosion volume + initial landslide body  
 486 volume + erosion volume



487

488 **Figure 6** (a) Landslide locations in Washington and Colorado states. Coordinates next to each site are WGS84.  
 489 Shaded DEMs of each site are shown at the same scale. (b) Observed average erosion rate per unit landslide length  
 490 ( $\bar{E}/\ell$ ) relative to the observed average-maximum grainsize. Error bars indicate standard deviation. (c) Underlying  
 491 topographic slope of observed deposition locations.

## 492 5.2 Model setup and field parameterization

493 Each model was set up on a 10-meter grid representation of the pre-event DEM. The extent of the [initial mass wasting](#)  
 494 [source material \(e.g., the initial landslide body\)](#) mass-wasting-source-material, which in all cases was a landslide, was  
 495 interpreted from a combination of lidar, air-photo and field observations. At all locations, we use [Equation \(13\)](#) to  
 496 approximate shear stress. We field-surveyed each site, noting the maximum flow thickness, typical deposition and  
 497 erosion depths and the size of the largest grains in the runout deposits.

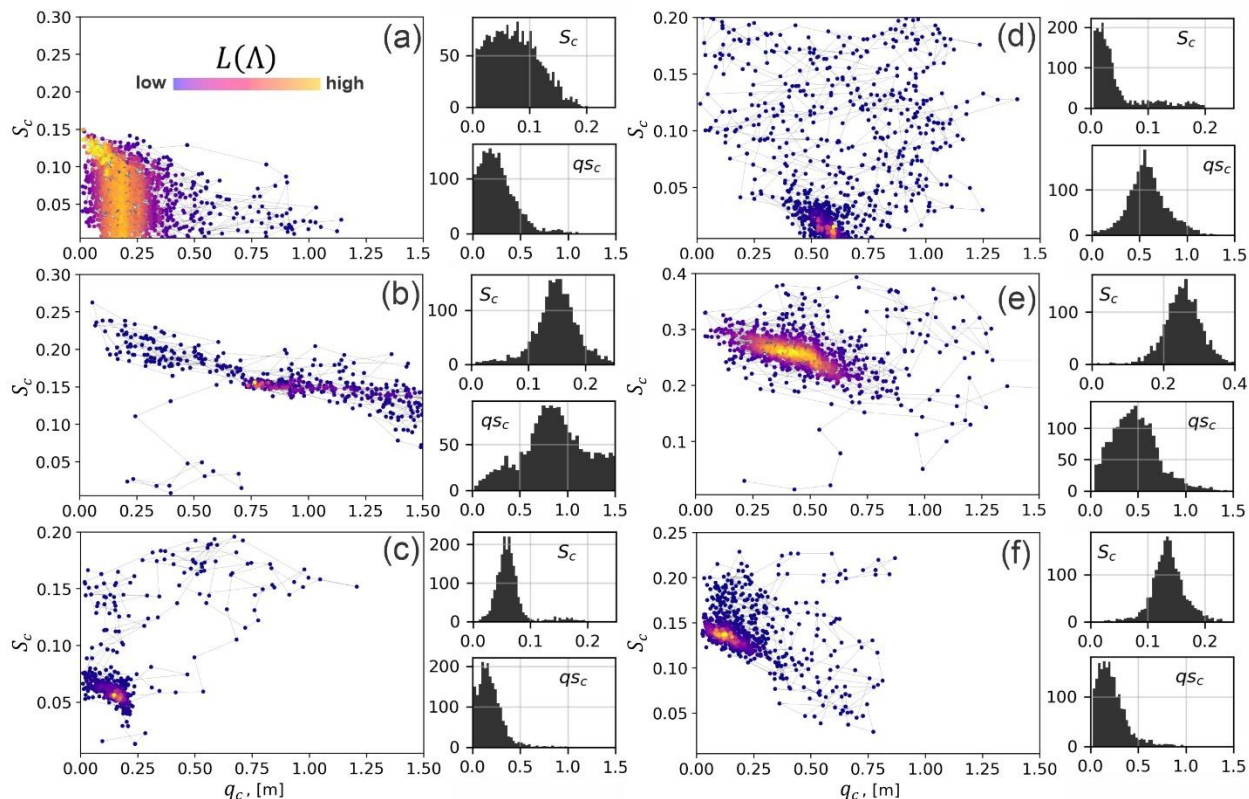
498 We estimated parameter values from these field and remote observations (See Table 1). A site-specific value for  $k$   
499 was determined as a function of the observed average erosion depth (determined as total erosion volume divided by  
500 the erosion area,  $\bar{E}$ ) relative to [the length of the runout debris, which we approximated as the length of the initial](#)  
501 [landslide body-the landslide length](#) ( $\ell$ ). Further details are described in [the the Supplementary MaterialAppendix](#).  
502 The [volume of the initial mass-wasting source material \(e.g., the initial-landslide body\)](#) ranged in volume from 400 to  
503 110,000 m<sup>3</sup> across sites. At all sites, erosion and subsequent entrainment added to the total mobilized volume (initial  
504 landslide [body](#) + erosion volume-), but the contribution was highly variable. The erosion volume divided by the total  
505 mobilized volume was as low as 0.19 at the Cascade Mountain, 2022 landslide to as high as 0.97 at the Olympic  
506 Mountain landslides (Table 1).  
507 The average maximum grain size varied from 0.2 m at the Black hills sites to nearly 1 m at the Rocky Mountain Site  
508 (Figure 6b, Table 1). Values of  $\bar{E}/\ell$  ranged from 0.007 to 0.041 [m/m] with the highest rate occurring at the Rocky  
509 Mountain landslide and the lowest at the Black Hills sites. [Details on grain-size samples and data collected in the field](#)  
510 [are described in the Supplementary Material](#). In terms of growth factors (average volumetric erosion per unit length  
511 of the erosion-dominated region of the runout path, Hungr et al. 1984; Reid et al., 2016) values ranged from 10 m<sup>3</sup>/m  
512 at the Black Hills South site to 95 m<sup>3</sup>/m during the Rocky Mountain landslide (Table 1).  
513 The median values of topographic slopes at which observed deposition occurred (i.e.,  $\Delta\eta > 0$ ) ranged between [0.3-1](#)  
514 [and 0.4-3](#) across sites, while deposition was also observed in much steeper (>0.4) slopes, and much flatter slopes at  
515 some sites (Figure 6c) (Table 1). The slope of channel reaches where net deposition (cumulative erosion and  
516 deposition; e.g., Guthrie et al., 2010) was positive tended to be lowest at the Black Hills site (<1% to 10%) and highest  
517 at Rocky Mountain site (16% to 25%).  
518 We defined uniform prior distributions of  $S_c$  and  $q_c$  [based-on-the-field-observations](#) and then used the calibration utility  
519 to find the best-fit parameter values (parameter values corresponding to the highest  $L(\Lambda)$ ). Minimum and maximum  
520 values of  $S_c$  were initially estimated from the range of observed slope of areas of positive-net deposition (Table 1).  
521 Minimum and maximum values of  $q_c$  were set as 0.01 to 1.75, which roughly represents the range of minimum  
522 observed thickness of debris flow termini in the field at all of the validation sites. For the purpose of implementing  
523 the calibration utility, we prepared a DoD of each site. The DoD was determined either from repeated [lidar](#) or field  
524 observations as detailed in the Supplementary Material.

### 525 **5.3 Calibration and model performance**

526 Markov chains, colored according to the likelihood index,  $L(\Lambda)$  are plotted in the  $S_c$ -  $q_c$  domain, along with  
527 histograms of sampled  $S_c$  and  $q_c$  values for each landslide in Figure 7. Each Markov chain includes 2000 model  
528 iterations. The runtime for 2000 model iterations depended on model domain-[and](#), landslide size [and number of](#)  
529 [landslides modeled](#) but varied from roughly 1.5 [for the Cascade, 2022 landslide](#) to 6 hours [for the Olympic Mountain](#)  
530 [landslides](#) on a 2016 2.1 GHz Intel Core Xeon, 32 GB memory desktop. The chains show a wide array of sampling  
531 patterns and parameter ranges but broadly speaking, at all sites, the algorithm jumped within  $S_c$ -  $q_c$  space towards  
532 higher  $L(\Lambda)$ , to form bell-shaped posterior distributions for each parameter. Depending on the landslide type, the  
533 calibration algorithm converged on different  $S_c$ -  $q_c$  pairs. For example, at the Cascade Mountains site, the calibration



534 utility converged to smaller  $q_c$  and  $S_c$  values for the 2009 event (Figure 7a), which permitted thinner flows over lower  
 535 slopes and effectively made the 2009 modelled runout more mobile relative to the 2022 modelled runout (Figure 7b).  
 536 At the Rocky Mountains site (Figure 7e), a relatively high  $q_c$  value helps control lateral extent of the modelled runout  
 537 that in the field was controlled by standing trees (see Supplementary Material) (Figure 7e).



538  
 539 **Figure 7.** MWR calibration results for (a) Cascade Mountains, 2009; (b) Cascade Mountains, 2022, (c) Black Hills,  
 540 South; (d) Black Hills, North; (e) Rocky Mountains and; (f) Olympic Mountains. Each result shows a scatter plot of  
 541 the sampled  $S_c$  and  $q_c$  values, colored by their relative  $L(\Lambda)$  value. Note y-axis scale differs between plots. To the  
 542 right of each scatter plot are histograms of the iterated  $S_c$  and  $q_c$  parameters, which can be normalized to represent  
 543 an empirical PDF of the possible  $S_c$  and  $q_c$  values that calibrate MWR to the site. Note y-axis scale differs between  
 544 plots. Histogram y-axis is count and x-axis is  $S_c$  or  $q_c$ , as indicated on the histogram.

545  
 546 Profile plots of modelled  $Q_s$  and maps of the modelled planimetric runout extent, colored to indicate where the runout  
 547 matched ( $\alpha$ ), overestimated ( $\beta$ ) or underestimated ( $\gamma$ ) the observed runout are shown in Figure 8. Values of  $\Omega_T$  we  
 548 obtained with MWR are comparable or higher than reported values of  $\Omega_T$  in the literature that used a variety of models  
 549 (Gorr et al., 2022; Barnhart et al., 2021; Note, to compare  $\Omega_T$  values to those studies, subtract 1 from values reported  
 550 in this study). Across the sites, the volumetric error of the model,  $\Delta\eta_E$ , ranges between 6% and 15% (median 9.1%)  
 551 of the total mobilized volume from the observed DoD. An overall <10% volumetric error is reasonable considering  
 552 the low number of parameters required to calibrate MWR and that empirical estimates of total mobilized volume used  
 553 to run other runout models can vary by as much of an order of magnitude (e.g., Gartner et al., 2014; Barnhart et al.,  
 554 2021). Model performance in predicting volume flux along the runout profile was within similar error ranges. Except  
 555 for the Rocky Mountains site where MWR consistently modelled wider-than-observed flow, the cumulative flow error

556 along the runout profile ( $Q_{sE}$ ) were limited to 5%-19% of the mean cumulative flow determined from the observed  
557 DoD.

558 MWR generally successfully replicates observed sediment transport along the runout path via model parameterizations  
559 that are unique to each landslide. For example, the profile plots of  $Q_s$  at the Cascade Mountain site (Figure 8a and 8b)  
560 show that during the 2009 landslide, all of the runout material flowed past the first 750 meters of the runout path.  
561 During the 2022 landslide, material began to deposit just down slope of the initial landslide scar, as both observed and  
562 modelled  $Q_s$  reverse slope, indicating loss in downstream volume flux. Model comparisons in the Cascade Mountains  
563 site were limited to the upper 750 m of the hillslope because a large portion of the runout material was lost to fluvial  
564 erosion in the valley (see Supplementary Material).

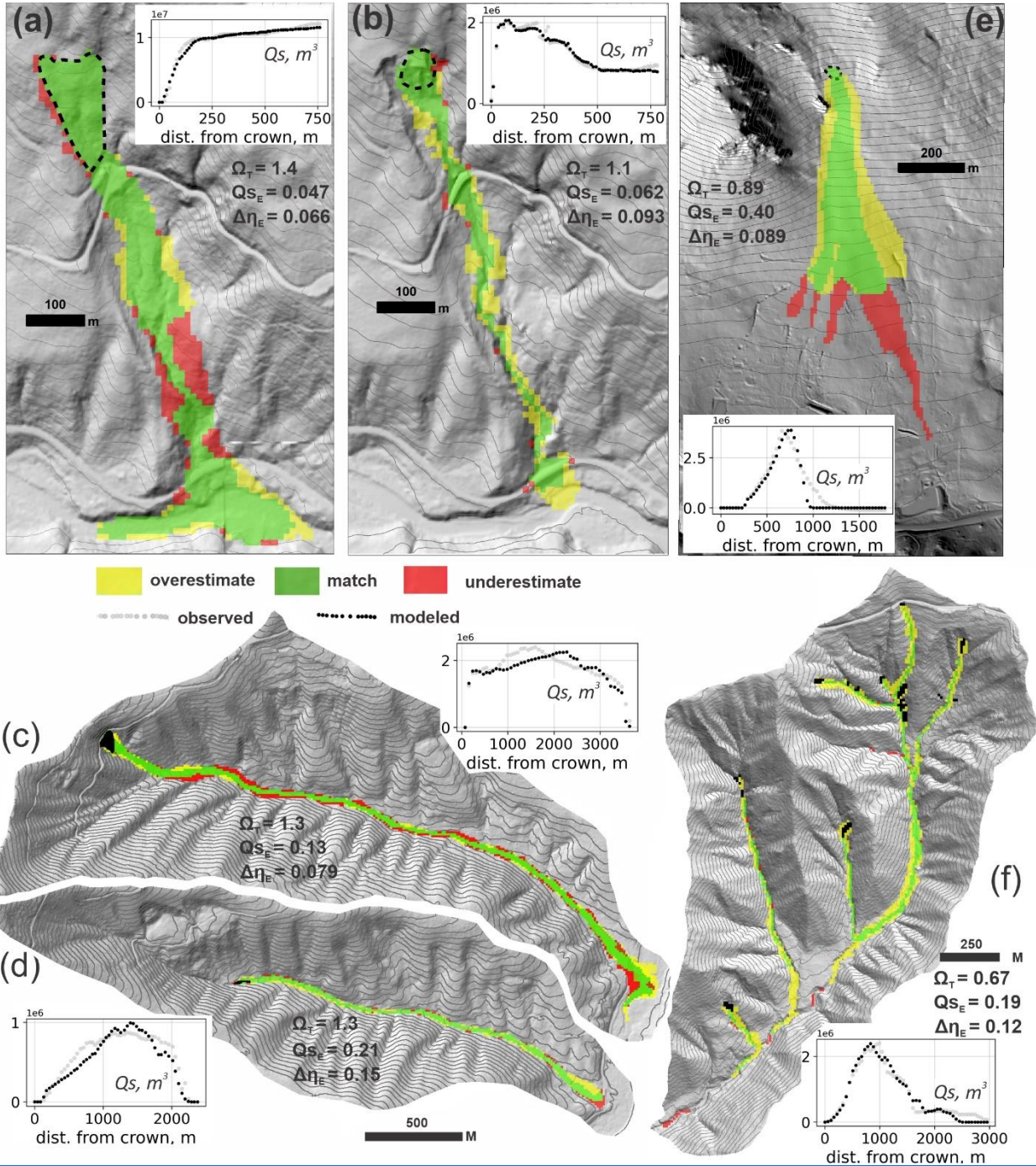
565 MWR also successfully replicates the observed sediment transport patterns at the Olympic Mountains site (profile plot  
566 of  $Q_s$  in Figure 8f) and to a lesser degree, the Rocky Mountain site (Figure 8e). This finding is notable, because at the  
567 Olympic Mountain site, observed runout extent and sediment depositional pattern were heavily impacted by woody  
568 debris. Similarly, at the Rocky Mountains site, the width of the runout appeared to be restricted by trees. (See  
569 Supplementary Material).

570 Using a fixed cell size of 10-m might have impacted model performance in some areas. MWR tended to over-estimate  
571 the runout width for small landslides like the Olympic Mountains and Cascade Mountains, 2022 sites (yellow zones  
572 in Figures 8f and 8b), likely because of the 10-m grid size used to represent the terrain. A 10-m DEM is generally  
573 accepted as a good balance between model detail and computational limitations (e.g., Horton et al. 2013). However,  
574 for small landslides, the 10-m grid is close to the size of the channels that controlled observed runout (Supplementary  
575 Material) and may not have accurately represented the terrain. Modelled flow was less topographically-constrained  
576 and tended to flow over a wider area of the terrain than observed in the more confined and smaller channels within  
577 the axis of the runout valleys.

578 Because MWR does not have an explicit representation of flow momentum, it may show poor performance in regions  
579 of the runout path where flow momentum is the primary control on runout extent. For example, at the Cascade  
580 Mountain, 2009 slide, ~~modelled extent misses a~~ MWR underestimates the slope-perpendicular flow over a bench  
581 ~~located along the east edge of the runout path~~ (large red zone in Figure 8a). Review of model behavior for this slide  
582 (Figure 9) shows how MWR successfully mimics diverging flow around a broad ridge upslope of the bench in the  
583 ~~middle of the runout path~~ (iteration  $t=28$  in Figure 9), but afterwards continues to follow topographic slope and  
584 converges too rapidly into a narrow ravine in the middle of the runout path along the west edge of the bench (iteration  
585  $t=40$  in Figure 9; compare to runout scar in air photo and underestimated region on topographic bench in Figure 8a).  
586 At the Rocky Mountains site, in addition to standing trees, the forward momentum of the runout may have also  
587 restricted lateral spread of the observed runout. Modelled runout is consistently too wide.

588 Overall, calibration was best at the Cascade Mountain, 2009 landslide (values of  $\Omega_T$  are highest and values of  $\Delta\eta_E$   
589 and  $Q_{sE}$  are lowest) and poorest at the Rocky Mountain and Olympic Mountain sites (Values of  $\Omega_T$  are lowest  $Q_{sE}$   
590 and  $\Delta\eta_E$  are highest). At both the Rocky Mountain and Olympic Mountain sites, because we lacked repeat lidar, we  
591 created the DoD from a map of field estimated erosion and deposition depths and estimated the pre-event DEM. The  
592 lower calibration scores may indicate that field estimated DoDs were not as accurate as those determined via lidar

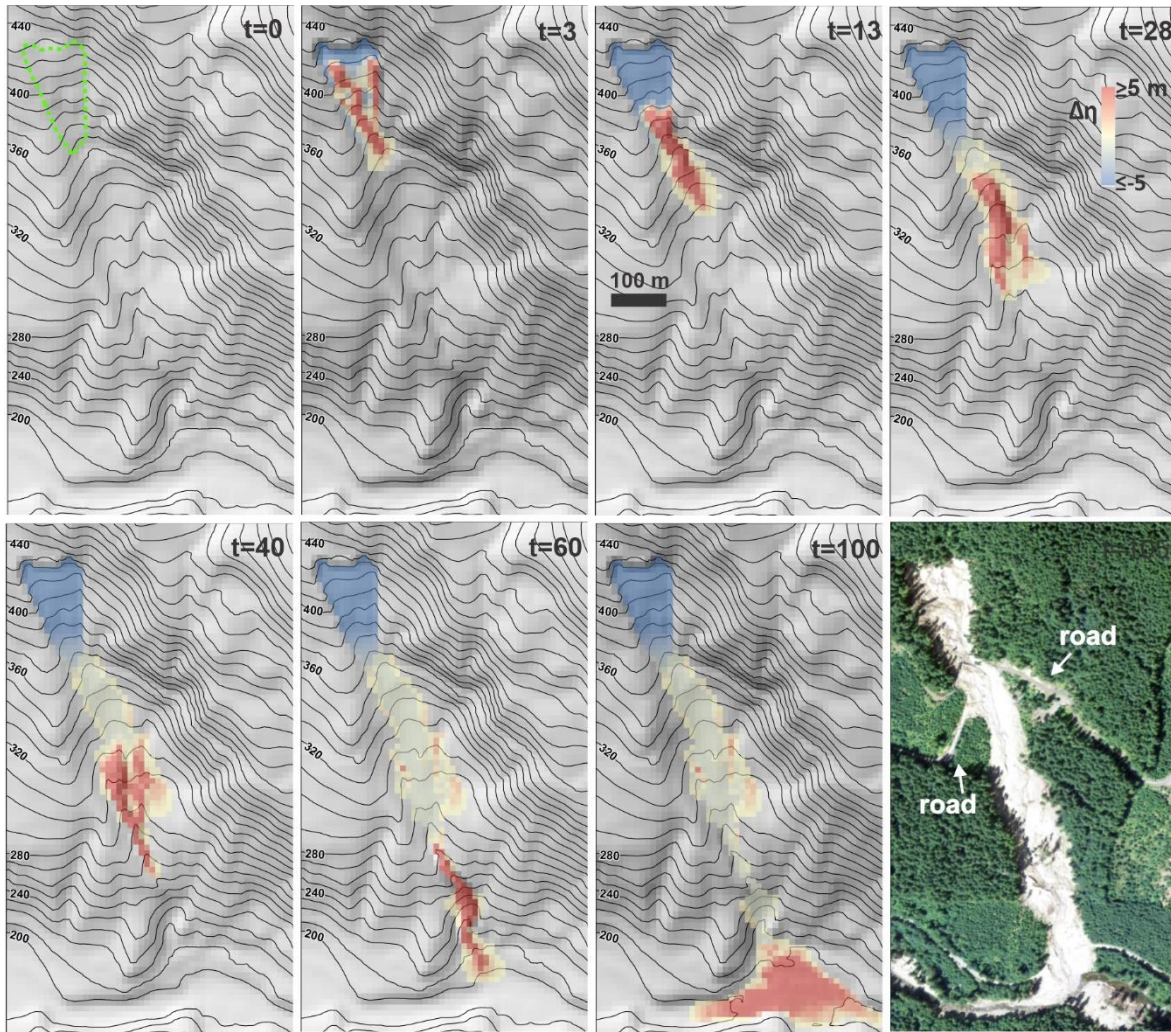
593 differencing. Another source of uncertainty that we have not addressed in our study is regolith thickness. Using  
 594 spatially accurate regolith thickness, rather than a uniform thickness, would likely improve MWR performance too.  
 595 Nonetheless, although imperfect, at most sites, MWR does not appear to have a strong systematic bias in modeled  
 596 output, which suggests that MWR may not have any structural weaknesses; however the consistent over-estimated  
 597 width on planar to divergent topography at the Rocky Mountain site requires further investigation at similar sites to  
 598 determine if this issue is due to calibration or the model.



599



600 **Figure 8.** Calibrated model performance as indicated by [maps of modeled runout extent](#), profile plots of [observed](#)  
 601 [and modeled cumulative sediment transport along the centerline of the runout path \( \$Q\_s\$ , see equation 28-\)](#) and  
 602 reported values of  $\Omega_T$ ,  $\Delta\eta_E$  and  $Q_{sE}$ . [Y-axis label for profile plots of  \$Q\_s\$  indicated on plot.](#) In all maps, up is north  
 603 except in (e), north is towards the left. (a) Cascade Mountains, 2009; (b) Cascade Mountains, 2022; (c) Black Hills,  
 604 North; (d) Black Hills, South; (e) Rocky Mountains; (f) Olympic Mountains.  
 605  
 606  
 607



608  
 609 **Figure 9.** Illustration of modeled runout [of the Cascade Mountains, 2009 landslide beginning from the initial](#)  
 610 [movement of the landslide body to final deposition in the river valley that demonstrates MWR response to](#)  
 611 [topography. at the Cascade Mountains, 2009 landslide. At iteration  \$t = 0\$ , Algorithm 1 determines the direction and](#)  
 612 [flux of the initial debritons over the slip surface of the landslide \(all nodes located in the landslide green dashed](#)  
 613 [polygon\).](#) Note how the landslide slip surface directs the initial flow. [In later iterations, Algorithm 2 routes the](#)  
 614 [debritons down slope, updating the debritons and the terrain. By the end of the modeled runout, a colluvial fan forms](#)  
 615 [at the base of the slope.](#) Topography lines reflect the underlying terrain, which is updated after each iteration. [Air](#)  
 616 [photo in last panel shows observed runout extent. Note that upper road is not part of the observed landslide runout](#)  
 617 [path. MWR successfully replicates diverging flow at iteration  \$t = 28\$  but misses a region of the observed runout](#)



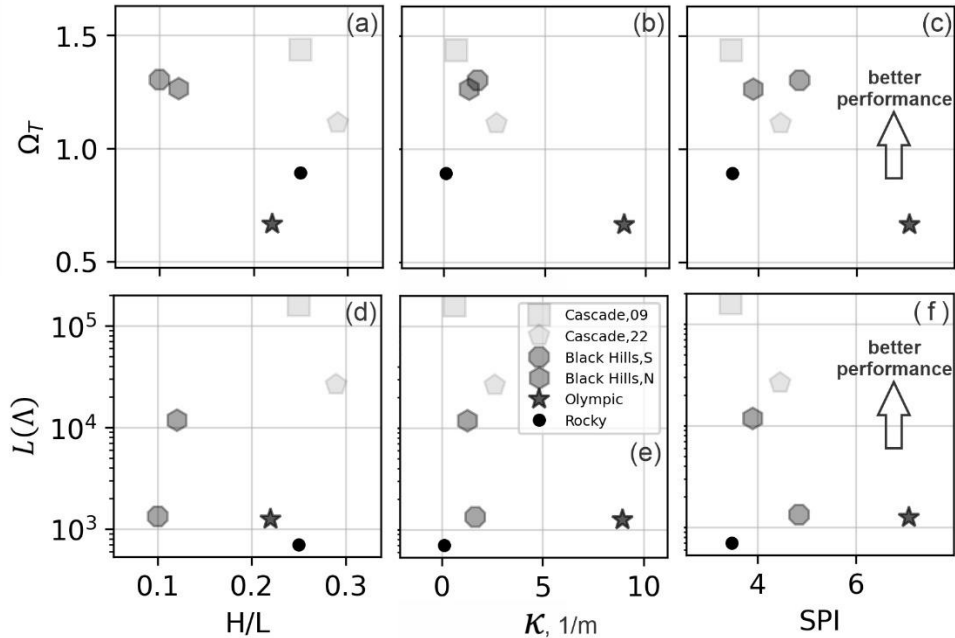
618 ~~path at iteration  $t = 40$  where momentum likely controlled flow direction (compare to runout scar in air photo and~~  
619 ~~underestimated region on topographic bench in Figure 8a)~~

620 To understand whether the ability to calibrate MWR systematically varies with topography of the runout path, we  
621 compared model performance with three topographic indices described by Chen & Yu (2011). The indices are  
622 computed from the terrain in the observed runout extent and include the relief ratio ( $H/LHA$ ), mean total curvature  
623 ( $\kappa$ ) and the mean specific stream power index ( $SPI$ ). The index  $H/LHA$  equals the average slope of the runout path  
624 (or relative relief), determined as the total topographic relief of the runout (measured from the center of the landslide  
625 to the end of the runout path) divided by the horizontal length of the runout and indicates the mobility of the runout.  
626 Index  $\kappa$  represents topographic convergence, which is the second derivative of the terrain surface, with increasingly  
627 positive values of index  $\kappa$  reflecting growing topographic convergence and concave-up channel profile (e.g.,  
628 Istanbuloglu et al., 2008). The index  $SPI$  is determined as the natural log of the product of the contributing area and  
629 slope. Indices  $\kappa$  and  $SPI$  are computed at each node in the runout extent ~~and the mean values are computed from all~~  
630 ~~nodes in the extent, and model performance is compared to the mean value.~~

631 Comparison of model performance with respect to the topographic indices in Figure 10 shows: slightly improved  
632 model performance over runout paths that are less convergent (~~lower  $SPI$  and  $\kappa$  values of the observed runout~~  
633 ~~path are lower~~) and on steeper terrain (higher  $H/LHA$ ) but neither trend is significant. The latter finding appears to  
634 be mostly a result of how well modelled sediment transport and topographic change ( $Q_{SE}$  and  $\Delta\eta_E$ ) replicated  
635 observed, as there does not appear to be a trend in  $\Omega_T$  with  $H/LHA$  and the two best performing models (both Cascade  
636 Mountain landslides) had the lowest (best)  $Q_{SE}$  values and low  $\Delta\eta_E$  values. Both findings are likely impacted by the  
637 grid size we used to represent terrain. As noted above, at all sites we used a 10-m grid, but at some sites 10-m doesn't  
638 quite capture the relief of channelized topography that controlled observed runout, leading to modelled runout that  
639 was considerably wider than observed and causing low  $\Omega_T$  value (this is especially true at the Olympic Mountains  
640 site, Figure 10a, b and c). Also, it is important to note that these indices were calculated for the extent of the observed  
641 debris flows and may not represent the topographic form that controlled the model.

642 In summary, using the calibration utility, we showed how ~~the~~ MWR can be calibrated to a range of different landslide  
643 types and runout terrains. To a certain degree, though calibration, MWR can be parameterized to compensate for  
644 deficiencies in the DEM or processes not explicitly represented in the model (momentum, woody debris). A  
645 relationship between model performance and topography was not eminent. We were unable to establish a clear pattern  
646 between calibration performance and topographic indices. This finding is likely a result of the contributions of  
647 numerous factors other than the terrain form, such as the DEM resolution, the quality of the DoD and importance of  
648 processes not explicitly included in the model that also impact performance.

649



650  
 651 **Figure 10.** Illustration of model calibration, as reflected by the posterior parameter likelihood  $L(\theta)$  and planimetric  
 652 fit ( $\Omega_T$ ) relative to topographic indices. There is no strong trend between the topographic indices and calibration  
 653 performance. [Note, curvature values are scaled by a factor of 100.](#)

654 **6. Discussion**

655 **6.1 Strategic testing of MWR for hazard mapping applications**

656 Having demonstrated basic model response to topography and that MWR can be calibrated to a variety of landslides  
 657 and runout terrains, we now strategically test MWR using the Cascade Mountain and Black Hills sites. Since both of  
 658 these sites include two separate landslides, we can thus test model performance by swapping best-fit model parameters  
 659 at each site, rerunning the models and comparing results with the original, calibrated results. At the Cascade Mountain  
 660 site, the 2009 and 2022 landslides originated on the same hillslope (Figure 8a and 8b). At Black Hills site, the two  
 661 landslides occurred on different hillslopes but in adjacent east-west oriented watersheds (Figure 8c and 8d).

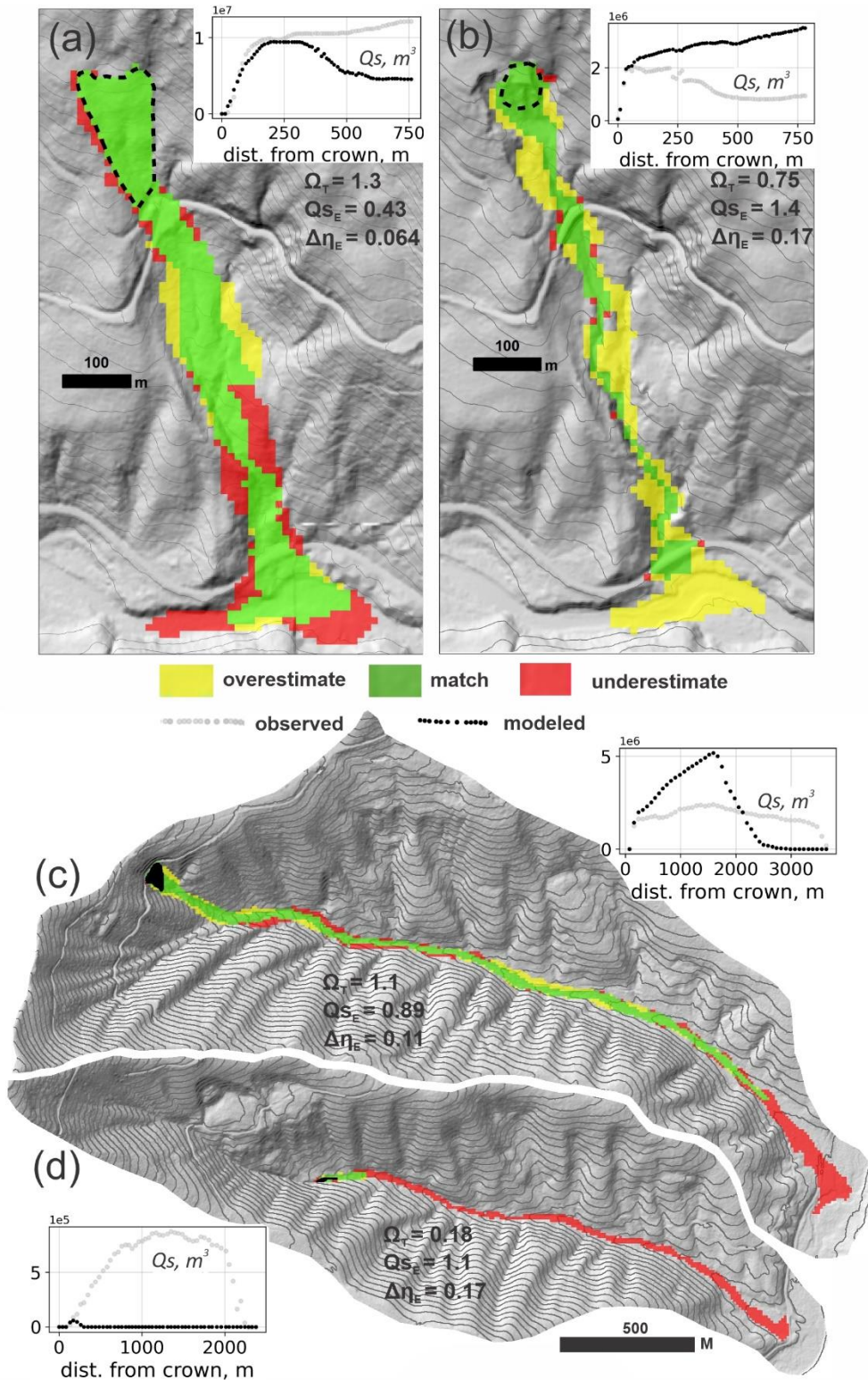
662 As shown in Figure 11, at three of the landslides (both Cascade Mountain landslides and the Black Hills, North  
 663 landslide), when the best-fit parameters from the other landslide are used to predict runout, the accuracy of modelled  
 664 runout planimetric extent drops but resultant  $\Omega_T$  values can still be as high or higher than values reported in other  
 665 studies (compare to equivalent  $\Omega_T$  values in Gorr et al., 2022 and Barnhart et al., 2021). In terms of modelled sediment  
 666 transport and topographic change, swapping best-fit parameters has a more substantial effect. At the Cascade  
 667 Mountain, 2009 landslide, using the 2022 best-fit parameter values causes about half of the modelled runout material  
 668 to prematurely deposit on the hillslope, reducing the amount of sediment that reaches the valley floor ( $Q_{sE}$  increases  
 669 by a factor of nine; Figure 11). Using the Cascade Mountain, 2009 parameter values on the Cascade Mountain, 2022  
 670 landslide (Figure 11b) increases modelled runout extent and results in nearly four times the entrainment and transport  
 671 of sediment to the valley floor, causing  $Q_{sE}$  to increase by a factor of 20 and  $\Delta\eta_E$  by 83%. At the Black Hills site,

672 using the South basin best-fit model parameters at the North basin causes  $Q_{sE}$  and  $\Delta\eta_E$  increase by 83% and 39%  
673 respectively (Figure 11c). Unlike the other three landslides, swapping best-fit parameters at the Black Hills, South  
674 landslide results in both large sediment transport and runout extent error because the North basin best-fit parameters  
675 cause modelled landslide to entrain too little and stop only a few hundred meters from the initial source area (Figure  
676 11d).

677 Although the need for calibration of MWR is a limitation for its transferability across sites, this limitation holds true  
678 for most physics-based models. Barnhart et al. (2021) compared the ability of three different detailed-mechanistic  
679 models to replicate an observed post-wildfire debris-flow runout event in California, USA. All three models used a  
680 shallow-water-equation-based approach that conserved both mass and momentum, representing the flow as either a  
681 single phase or double phase fluid. All models gave comparable results in simulating the event, suggesting that there  
682 may not be a “true” best model. Despite the high level of detail and processes explicitly included in each model, all  
683 models were sensitive to and required an estimate of the total mobilized volume, and the ability to replicate observed  
684 runout ultimately depended on [the selection calibration](#) of the parameters used to characterize debris flow properties.

685

686



687

688

689

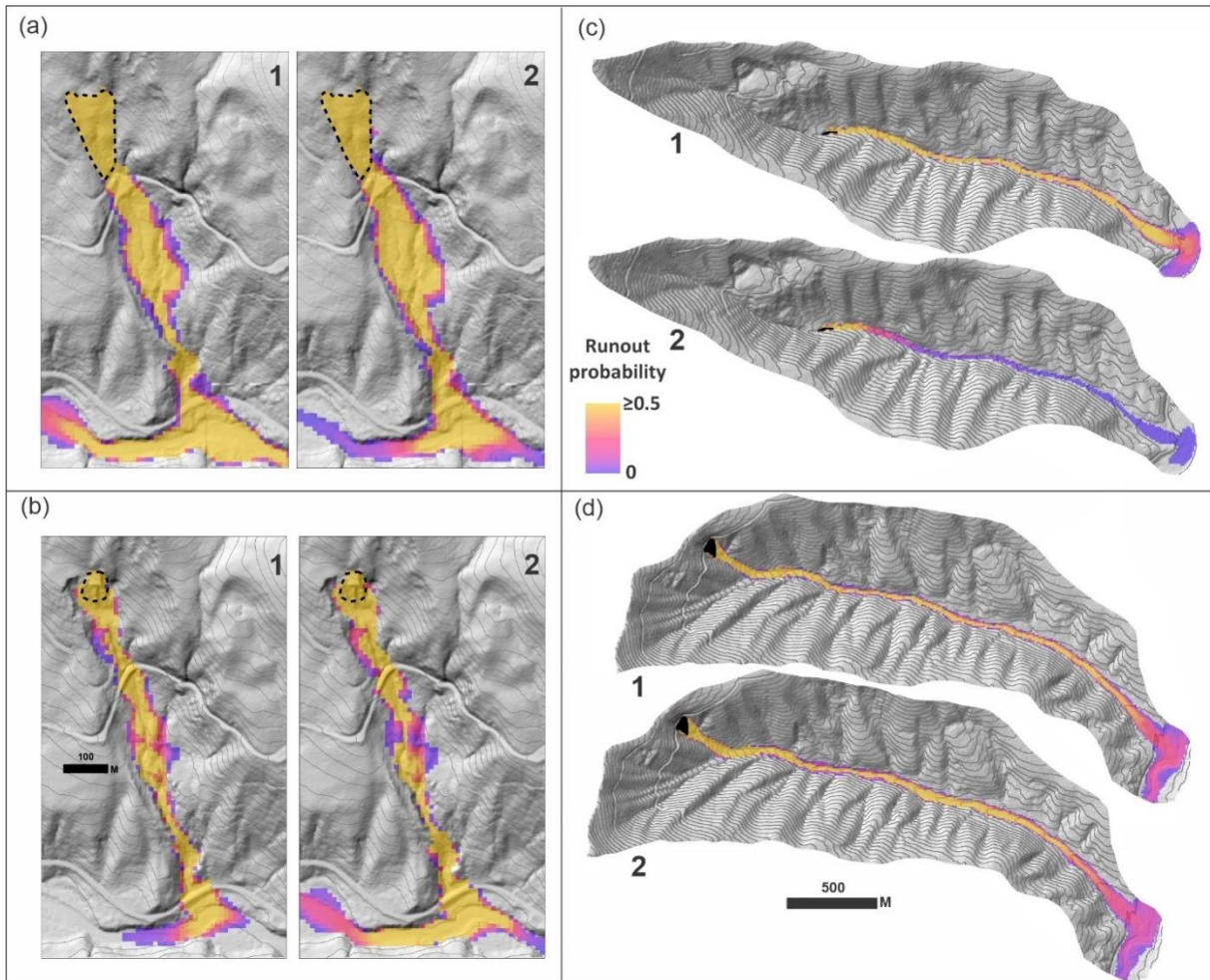
690

**Figure 11.** Model performance using the neighboring landslide parameter values, as indicated by modeled runout extent, profile plots of  $Q_s$ , reported values of  $\Omega_T$ ,  $\Delta\eta_E$  and  $Q_{SE}$ . Compare with Figure 8. (a) Cascade Mountain, 2009; (b) Cascade Mountain, 2022; (c) Black Hills, North; (d) Black Hills, South



691  
692  
693  
694  
695  
696  
697  
698

As landslide hazard models often forecast hazard probabilistically, an alternative test to simply swapping the best-fit parameters is to swap parameter PDFs determined from the calibration utility and compare probability of runout at each model node (equation 30). As shown in Figure 12, similar to the first test, at three of the landslides, using the parameter distribution associated with the neighbouring landslide results in relatively minor changes in whether runout is likely to occur versus not occur (probability of runout  $\geq 50\%$ ; Figures 12a, 12b and 12d). At the Black Hills South landslide, swapping parameter PDFs causes a large change in runout probability (Figure 12c).



699  
700  
701  
702  
703

**Figure 12.** Model tests by swapping parameter PDFs and comparing runout probability at the (a) Cascade Mountain, 2009; (b) Cascade Mountain, 2022; (c) Black Hills, South and; (d) Black Hills, North sites. (1) runout using parameter distributions of the site and (2) runout using parameter distributions of the neighboring site.

704 The results of these two tests suggest that ~~in most cases, once best fit parameters or parameter PDFs have been~~  
705 ~~established for a landslide, those parameter/PDF values may be useful for assessing runout extent but not useful for~~  
706 ~~sediment transport and topographic change prediction at nearby sites. site-specific calibration may be needed when~~  
707 ~~the user aims to apply MWR to sediment budget analyses; however, we suspect that this finding is a consequence of~~  
708 ~~testing the model at a site with very different landslide types and runout processes. At sites like the Cascade Mountain~~



709 [and Black Hills sites, which consisted of a diverse range of landslide processes including small, confined debris flows](#)  
710 [to large, unconfined debris avalanches, MWR may need to be calibrated to each type of landslide and predictive](#)  
711 [applications might involve applying the appropriate parameter set based on landslide type. In regions where landslide](#)  
712 [processes are relatively uniform \(like the Olympic Mountain site\), calibration to one landslide might be sufficient to](#)  
713 [predict the depositional patterns and sediment transport at another. Finally, as noted in Section 3.1, we found numerous](#)  
714 [parameter combinations allowed MWR to match observed runout extent. This finding suggests that if the project aim](#)  
715 [is limited to an evaluation of runout extent, model calibration to the site may not be as critical and parameter values](#)  
716 [from calibration to nearby landslides or even globally-available repeated DEMs and airphotos that show the slope of](#)  
717 [past landslide deposits \(for  \$S\_c\$ \) and how thick their frontal lobes are at the point of deposition \(for  \$q\_c\$ \), might be](#)  
718 [sufficient. However, we suspect that these results are a consequence of comparing very different landslide types and](#)  
719 [runout processes. In regions where landslide processes are relatively uniform \(like the Olympic Mountain site\),](#)  
720 [calibration to one landslide might be sufficient to predict the depositional patterns of another. At sites like the Cascade](#)  
721 [Mountain and Black Hills sites, which consisted of a diverse range of landslide processes including small, confined](#)  
722 [debris flows to large, unconfined debris avalanches, MWR may need to be calibrated to each type of landslide and](#)  
723 [predictive applications might involve applying the appropriate parameter set based on landslide type.](#)

## 724 **6.2. MassWastingRunout probability applications**

725 In this section we briefly demonstrate how to determine runout probability from a probabilistically determined  
726 landslide hazard map or a specific, potentially unstable slope using MWR. The first application may be appropriate  
727 for watershed- to regional-scale runout hazard assessments. The second application is an example hazard assessment  
728 for a potentially unstable hillslope. Both applications are demonstrated at the Olympic Mountain site where landslide  
729 size and type tended to be relatively uniform and parameter PDFs determined through calibration may therefore  
730 represent typical runout processes in the basin.

### 731 **6.2.1. Runout probability from a landslide hazard map**

732 To determine runout probability from a landslide hazard map, we ran MWR Probability using ~~option~~ [Option 3](#), reading  
733 a series of mapped landslide source areas created by an externally run Monte Carlo landslide initiation model. For the  
734 landslide initiation model, we used LandslideProbability, an existing component in Landlab that computes landslide  
735 probability by iteratively calculating Factor-of-Safety ( $FS$ : ratio of the resisting to the driving forces) at each node on  
736 the raster model grid  $Np$  times from randomly selected soil (regolith) hydrology properties (e.g., soil depth, saturated  
737 hydraulic conductivity) soil strength (friction angle, cohesion) and recharge rates (precipitation input rate minus  
738 evapotranspiration and soil storage). Landslide probability at a node is defined as the number of times  $FS < 1$  divided  
739 by  $Np$ .

740 We first ran LandslideProbability using a 50-year precipitation event (WRCC, 2017) to determine landslide  
741 probability (Figure 13a) over the entire Olympic Mountains model domain and create the series of  $Np$  FS maps.  
742 Details on the LandslideProbability setup are included in the Supplementary Material. We then read the series of FS  
743 maps into MWR Probability, treating all nodes with  $FS < 1$  as a landslide source, and ran MWR  $Np$  times. Each

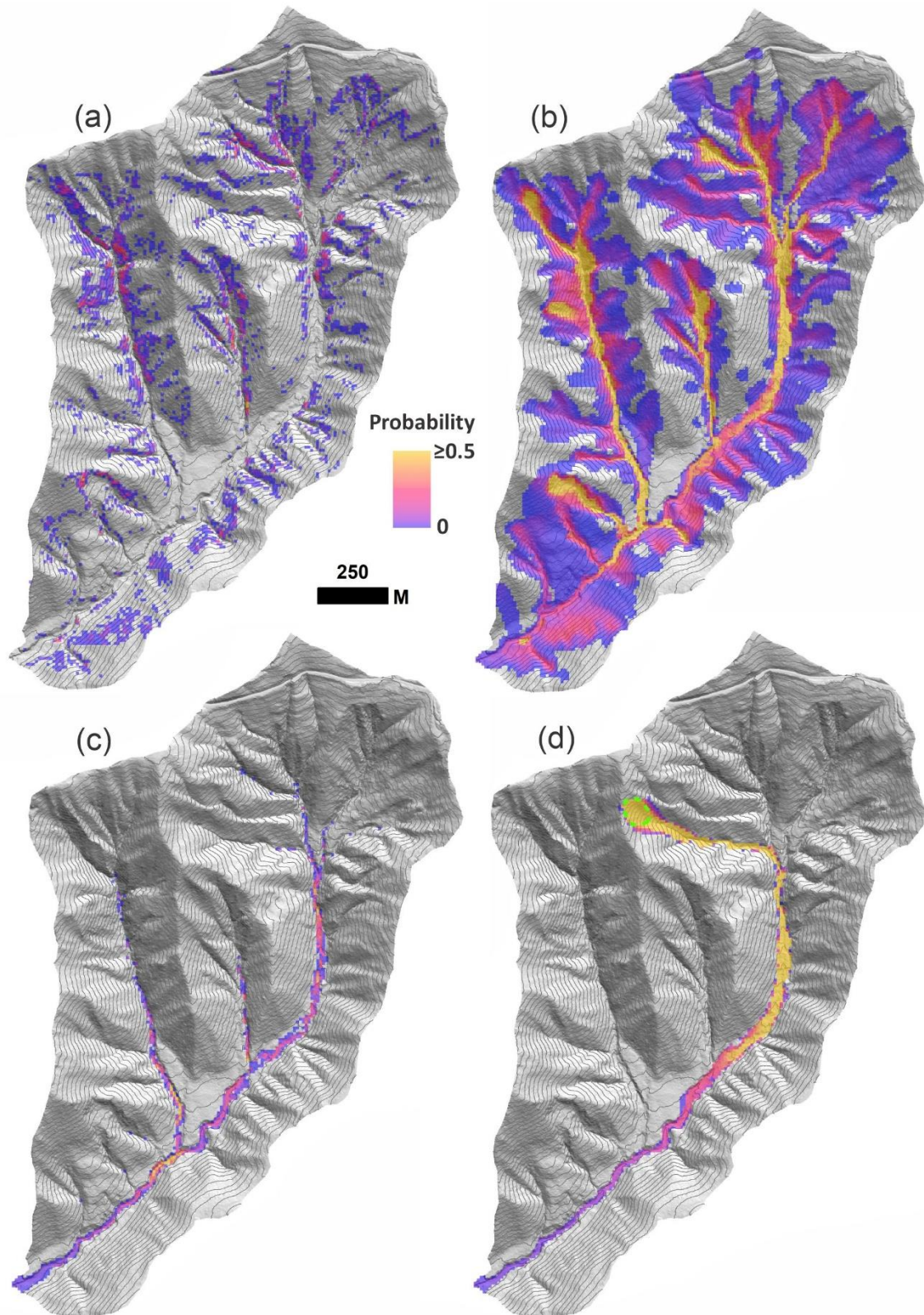
744 iteration, MWR read a new *FS* map and randomly selected a new set of parameter values from  $S_c$ - $q_c$  parameter PDFs  
745 created by the calibration utility.

746 Runout probability results are illustrated in Figure 13b and show that the probability of runout is high in many of the  
747 second order channels but low at the basin outlet. As discussed in Section 3, the probability of aggradation or erosion  
748 caused by the runout can also be determined by adjusting the numerator of [Eq. \(30\)](#) and the probability of deposition  
749 greater than 1 meter is shown in Figure 13c. In this example, in addition to MWR parameter uncertainty, runout  
750 probability reflects uncertainty in landslide size and location caused by a 50-year precipitation event.

### 751 **6.2.2 Runout probability for a specific, potentially unstable slope**

752 When field evidence or other data indicate that a specific hillslope may be potentially unstable, but the exact area of  
753 a potential landslide on that slope is unknown, MWR can be used to generate a hazard estimate that takes into account  
754 the uncertainty in the landslide area. For this application, MWR Probability is run using [Option \(2\)](#), which requires  
755 a polygon representing the extent of the potentially unstable slope. [We designated a 0.6 ha, convergent hillslope in the](#)  
756 [headwaters of the Olympic Mountains site as a potentially unstable slope \(Figure 13d\)](#). For each model repetition, a  
757 landslide area can form anywhere within the potentially unstable slope and is at least as large as a user defined  
758 minimum size but no larger than the potentially unstable slope.

759 ~~As an example application of using MWR Probability option (2), we designated a 0.6 ha, convergent hillslope in the~~  
760 ~~headwaters of the Olympic Mountains site as a potentially unstable slope and modelled runout probability, again using~~  
761  ~~$N_p = 1000$  (Figure 13d).~~ This example shows that, given uncertainty in the landslide size and location, and  
762 uncertainty in ~~calibrated parameterization of~~ MWR [parameterization](#), if a landslide were to initiate on the potentially  
763 unstable slope, the probability of the runout reaching the basin outlet is less than 5%.



764  
765  
766  
767

**Figure 13.** Olympic Mountain site: (a) Landslide probability,  $P(FS \leq 1)$ . (b) Corresponding runout probability,  $P(\Delta\eta)$ . (c) Probability of deposition greater than 1 m and (d) Runout probability for the potentially unstable slope (green-dashed polygon).

## 768 7.0 Concluding remarks

769 In this study, we described, calibrated and tested MassWastingRunout (MWR), a new cellular-~~automata-automaton~~  
770 landslide runout model that combines the functionality of simple runout algorithms used in landscape evolution and  
771 watershed sediment yield models (WSMs) with the predictive detail typical of runout models used for landslide  
772 inundation hazard mapping. MWR is implemented in Python as a component for the Landlab earth surface modelling  
773 toolkit and is designed for probabilistic landslide hazard assessments, sediment transport and landscape evolution  
774 applications. MWR includes a Markov Chain Monte Carlo calibration utility that determines the best-fit parameter  
775 values for a site as well as empirical Probability Density Functions (PDF) of the parameter values. MWR also includes  
776 a utility called MWR Probability that takes the PDF output from the calibration utility to ~~model-determine~~ runout  
777 probability.

778 Results ~~show indicate~~ that despite its simple conceptualization, ~~MWR shows skill in modeling the final runout extent,~~  
779 ~~sediment transport and topographic change associated with a landslide.~~ ~~MWR can replicate observed erosion,~~  
780 ~~deposition and sediment transport patterns.~~ ~~MWR needs only the location and geometry of an initial landslide source~~  
781 ~~area to model the entire runout process,~~ ~~and two parameters (critical slope,  $S_c$ , and a threshold flux for deposition,~~  
782  ~~$q_c$ ) to model the entire runout process.~~ A notable finding of this paper is that MWR modeled runout did not have any  
783 ~~strong systematic bias in predictions (toward unrealistically short or wide flows, for example), which suggests that~~  
784 ~~MWR may not have any structural weaknesses.~~ When compared to other models capable of replicating ~~observed~~  
785 ~~landslide~~ inundation patterns ~~of observed runout events~~, the strength of MWR lies in its ~~potential-computational~~  
786 ~~efficiency,~~ use of field-inferable parameters, ~~limited reliance on calibration parameters (only two, critical slope,  $S_c$ ,~~  
787 ~~and a threshold flux for deposition,  $q_c$ ) and,~~ its ability to internally estimate the total mobilized volume (~~initial~~  
788 ~~landslide body + erosion volume~~ ) and its relatively parsimonious model design. ~~MWR needs only the location and~~  
789 ~~geometry of an initial landslide source area to model the entire runout process~~  
790 ~~MWR can be calibrated to a site using just two parameters (critical slope,  $S_c$ , and a threshold flux for deposition,  $q_c$ )~~  
791 ~~and the MWR calibration utility enables the user to calibrate the model for a watershed within several hours on a~~  
792 ~~standard desktop (Section 5.3).~~ ~~Although the predictive power of MWR hinges on calibration—a common~~  
793 ~~requirement for mechanistic models—its reliance on two calibration parameters serves to constrain model uncertainty.~~  
794 ~~Site-specific calibration is may be needed when MWR is used for sediment budget analysis,~~ but if the aim is limited  
795 ~~to mapping- runout extent, it may be possible to- infer parameterization from nearby landslides or possibly from~~  
796 ~~globally available repeated DEMs and air photos that shows where past mass-wasting flows have stopped (for  $S_c$ ) and~~  
797 ~~how thick their frontal lobes are at the point of deposition (for  $q_c$ ).~~ Nonetheless, as a rules-based, cellular-automaton  
798 ~~model, MWR is not designed to accurately simulate flow depth. For accurate flow depths or debris flow impact forces,~~  
799 ~~a detailed-mechanistic modeling approach should be used.~~

800  
801 MWR shows a rich set of intuitive responses to topographic curvature and slope ~~and model performance over a range~~  
802 ~~of landslide and landscape conditions.~~ ~~When calibrated to the runout of six different observed landslides across the~~  
803 ~~four sites we used for this study was sufficiently controlled with the two calibration parameters.~~ When calibrated to  
804 ~~each individual site,~~ the volumetric error of MWR,  $\Delta\eta_E$ , ranged between 6% and 15% (median 9.1%) of the observed



805 total mobilized volume. Except for the Rocky Mountains site where MWR consistently modelled wider-than-observed  
 806 flow, the cumulative flow error along the runout profile ( $Q_{sE}$ ) were limited to 5%-19% of the mean cumulative flow  
 807 determined from the observed [DEM-of-Difference \(DoD\)](#). These are considered acceptable levels of performance  
 808 given that the total mobilized volume of many debris flow models assume an order of magnitude range of confidence.  
 809 [A notable finding of this paper is that MWR modeled runout did not have any strong systematic bias in predictions](#)  
 810 [\(toward unrealistically short or wide flows, for example\), which suggests that MWR may not have any structural](#)  
 811 [weaknesses is structurally sound. However, MWR may underperform compared to mechanistic models when flow](#)  
 812 [momentum is the primary driver of runout extent. \(e.g., in areas of slope-perpendicular flow\).](#)

813  
 814 ~~[Once MWR is calibrated to runout observations, it can be linked to other landslide hazard models and may be useful](#)~~  
 815 ~~[as a regional runout hazard mapping tool in areas with relatively uniform landslide processes. In this study we showed](#)~~  
 816 ~~[how to use MWR to map debris flow hazard for an expert defined potentially unstable slope and for a landslide hazard](#)~~  
 817 ~~[map produced from an externally run Monte Carlo landslide initiation model \(Figure 13\).](#)~~

818 As a component of the Landlab earth surface modelling toolkit, MWR is designed to be compatible with other models.  
 819 MWR can be readily coupled with a landslide initiation model (e.g., LandslideProbability) and geomorphic transport  
 820 laws for hillslope diffusion and fluvial incision to investigate the role of landslides and their runout on long-term  
 821 landscape evolution. [In this study we showed how to couple MWR with LandslideProbability to map debris flow](#)  
 822 [hazard when landslide initiation location is uncertain.](#) ~~[showed how to use MWR to map debris flow hazard for an](#)~~  
 823 ~~[expert defined potentially unstable slope and for a landslide hazard map produced from an externally run Monte Carlo](#)~~  
 824 ~~[landslide initiation model \(Figure 13\).](#)~~ ~~[We did not explore the use of MWR in landscape evolution or sediment yield](#)~~  
 825 ~~[models in this study, however its ability to replicate observed topographic change and sediment transport at multiple](#)~~  
 826 ~~[sites shows promise for this application. Future studies will explore large-scale application in landscape evolution or](#)~~  
 827 ~~[sediment yield models, and characterize model parameters for different geologic and hydroclimatic conditions.](#)~~ The  
 828 use of a calibrated runout model in WSMs might allow for region-specific and more insightful predictions of landslide  
 829 impact on landscape morphology and watershed-scale sediment dynamics.

### 830 [Appendix A - Determination of \$k\$](#)

831 [The average erosion depth caused by the observed runout \( \$\bar{E}\$ \) can be determined from the DoD as the total erosion](#)  
 832 [volume \( \$\sum E \Delta x^2\$ \) divided by the erosion area \( \$A\$ \) in the DoD:](#)

$$834 \quad \bar{E} = \frac{\sum E \Delta x^2}{A} \tag{A1}$$

835 [where  \$\sum E \Delta x^2\$  and  \$A\$  exclude the initial landslide body volume and area, areas of deposition \( \$\Delta \eta > 0\$ \) and areas](#)  
 836 [with no change in elevation \( \$\Delta \eta = 0\$ \). In terms of the debriton conceptualization used in MWR,  \$\bar{E}\$  can also be](#)  
 837 [written as a function of the mean number of times a debriton would need to pass over a grid cell \( \$\bar{n}\$ \) multiplied by an](#)  
 838 [average erosion depth per debriton \( \$\bar{h}\_e\$ \) to equal  \$\bar{E}\$  as:](#)

$$839 \quad \bar{E} = \bar{n} \bar{h}_e \tag{A2}$$



840 [An estimate for  \$\bar{n}\$  can be determined from the average length of the runout material, which we approximate simply](#)  
 841 [as the mapped landslide length \( \$\ell\$ \) divided by the cell width:](#)

$$842 \quad \bar{n} = \frac{\ell}{\Delta x} \quad (A3)$$

843 [Note that if the observed runout formed as a result of multiple landslides \(as was the case at the Olympic Mountain](#)  
 844 [site, see Supplementary Material\), then  \$\ell\$  was determined as the sum of the initial landslide body lengths. Also, as](#)  
 845 [the debritons move down slopes in excess of  \$S\_c\$ , they entrain material, split, and spread, and the runout material](#)  
 846 [tends to lengthen. Using the initial landslide length to represent the runout length thus represents a minimum value](#)  
 847 [for  \$\bar{n}\$  and if needed, \(A2\) can be multiplied by a coefficient to scale  \$\ell\$  into a more representative runout length.](#)  
 848 [Combining \(A2\) and \(A3\),  \$\bar{h}\_e\$  can be defined as the average erosion rate per unit length of runout debris \( \$\bar{E}/\ell\$ \) times](#)  
 849 [the cell width:](#)

$$850 \quad \bar{h}_e = \frac{\bar{E} \Delta x}{\ell} \quad (A4)$$

851 [Rewriting equation \(11\) as a function of the average shear stress in the erosion-dominated reaches of the runout path](#)  
 852 [\( \$\bar{\tau}\$ \) and assuming  \$\tau\_c \cong 0\$ , debris flow erodibility parameter  \$k\$  can be estimated as:](#)

$$853 \quad k = \frac{\bar{h}_e}{\bar{\tau} f} \quad (A5)$$

854 [To solve for  \$k\$ , we estimated  \$\bar{\tau}\$  from field-approximated debris flow depth and channel slope measurements in the](#)  
 855 [erosion-dominated reaches of the runout path. To estimate flow depth, we used the height of scour marks on the](#)  
 856 [channel wall or tree trunks, above the channel bed \(Table 1\). We used \(13\) to define  \$\bar{\tau}\$ . For  \$D\_s\$ , we used the average](#)  
 857 [maximum grain size observed over the whole runout path. If  \$\tau\$  is defined as a function of grain-collision dependent](#)  
 858 [shear stress approach \(13\) and  \$k\$  is determined as a function of  \$f\$ , as in \(A5\), the impact of  \$f\$  on model behavior is](#)  
 859 [relatively small.](#)

## 860 **8.0 Notation**

861	$q_{R_i}$	[m]	debris flux from a node to each of the node $i$ -th receiver nodes
862	$q_O$	[m]	the total out-going debris flux
863	$Nr$		the number of receiving nodes of node $n$
864	$S_i$		the underlying topographic slope ( $\tan \theta$ ) to each of the node $i$ -th receiver nodes
865	$a$		exponent in (1) that controls how flow is distributed to downslope nodes
866	$q_I$	[m]	The total incoming flux
867	$Nd$		number of donors nodes to a node
868	$q_{D_j}$	[m]	the flux from node $D_j$ (the $j$ -th donor node)
869	$h$	[m]	flow depth at node, adjusted to be no more than $h_{max}$
870	$h_{max}$	[m]	the maximum observed flow depth
871	$A$	[m]	aggradation depth
872	$S_c$		critical slope
873	$S$		steepest slope to the node's eight neighbouring nodes
874	$\Delta x$	[m]	cell length
875	$A_{p N_a}$	[m]	potential aggradation depth that forms a deposit that spreads over $N_a$ consecutive nodes

876	$A_{p,i}$	[m]	i-th deposition amount in the deposit illustrated in Figure 4
877	$N_a$		number of nodes $q_s^I$ is assumed to spreads over
878	$E$	[m]	erosion depth
879	$h_r$	[m]	regolith depth
880	$h_e$	[m]	potential erosion depth
881	$\theta$	[°]	topographic slope used to determine shear stress, equal to $\tan^{-1}(S)$
882	$\tau$	[Pa]	basal shear stress
883	$\tau_c$	[Pa]	critical shear stress of the regolith
884	$k$		erodibility parameter in (11)
885	$f$		exponent, controls the non-linearity of $h_e$ in (11)
886	$\rho$	[kg/m <sup>3</sup> ]	density of runout material
887	$\sigma$	[Pa]	normal stress at basal surface
888	$\varphi$		tangent of collision angle between grains, measured from the vertical axis
889	$v_s$		volumetric solids concentration
890	$\rho_s$	[kg/m <sup>3</sup> ]	density of solids
891	$D_s$	[m]	characteristic particle diameter
892	$u$	[m/s]	depth average flow velocity
893	$z$	[m]	depth below the flow surface
894	$u^*$		shear velocity
895	$g$	[m/s <sup>2</sup> ]	acceleration due to gravity
896	$\Delta\eta$	[m]	change in elevation at node
897	$q_D$		<a href="#">a vector containing all <math>q_{D,j}</math> sent to the node</a>
898	$\xi_D$		<a href="#">a vector containing the incoming attribute values for each <math>q_{D,j}</math></a>
899	$\xi_D$		attribute value delivered to the node
900	$\xi_R$		attribute value sent to receiver nodes
901	$\xi$		attribute value at node
902	$\eta$	[m]	<a href="#">topographic elevation</a>
903	$\Lambda$		parameter set
904	$L(\Lambda)$		likelihood of parameter set
905	$p(\Lambda)$		prior probability of parameter set
906	$\Omega_T$		<a href="#">the Lee-Salle index for evaluating model planimetric fit <math>\omega</math>-metric, nondimensional</a>
907	$\alpha$	[m <sup>2</sup> ]	modelled area of matching extent (compared to observed runout extent)
908	$\beta$	[m <sup>2</sup> ]	modelled area of overestimated extent
909	$\gamma$	[m <sup>2</sup> ]	modelled area of underestimated extent
910	$\Delta\eta_E$		volumetric error of the modelled topographic change relative to the observed total mobilized volume, fraction.
911	$V$	[m <sup>3</sup> ]	observed total mobilized volume
912	$p$		the number of nodes in the modelled runout extent
913	$\Delta\eta_{Mi}$	[m]	the modelled topographic change [m] at the i-th node within the runout extent
914	$\Delta\eta_{Oi}$	[m]	the observed topographic change [m] at the i-th node within the runout extent
915			
916			
917	$Q_{sE}$		mean-modelled-cumulative flow error along the runout path relative to the observed mean cumulative flow, fraction.
918			
919	$j$		<a href="#">index used to represent each node along a profile of the runout path.</a>
920	$\Delta\eta_{ij}$	[m]	<a href="#">topographic change [m] at the i-th node located upstream of node j</a>
921	$u_j$		<a href="#">total number of all nodes located upstream of node j</a>
922	$r$		<a href="#">the number of nodes along the center line of the runout path</a>
923	$Q_{s\dot{j}}$	[m <sup>3</sup> ]	the cumulative debris flow volume ( $Q_s$ ) at each node, $j$ ; <a href="#">along the center line of the runout path</a>
924			
925	$Q_{sO}$	[m <sup>3</sup> ]	<a href="#">the observed cumulative debris flow volume (<math>Q_s</math>) at each node, j</a>
926	$Q_{sM}$	[m <sup>3</sup> ]	<a href="#">the modeled cumulative debris flow volume (<math>Q_s</math>) at each node, j</a>
927	$\Delta\eta_{ij}$	[m]	the topographic change [m] at the i-th node located upstream of node j
928	$u_j$		the total number of all nodes located upstream of j

929	$\overline{Q}_{so}$	[m <sup>3</sup> ]	the observed mean cumulative flow
930	$P(\Delta\eta)$		
931	$\overline{E}/\ell$	[m/m]	average erosion per unit length of runout debris
932	$P(\Delta\eta)$		probability of runout, expressed as the probability that the elevation of a node changes
933			probability of runout at a model node
934	#		number of
935	$Np$		number Monte Carlo iterations used to determine probability
936	$A$	[m <sup>2</sup> ]	erosion area of the observed or modeled runout
937	$\overline{E}$	[m]	average erosion depth caused by the runout
938	$\sum E\Delta x^2$	[m <sup>3</sup> ]	the total erosion volume
939	$\overline{n}$		mean number of times a debriton would need to pass over a grid cell multiplied by an
940			average erosion depth per debriton to equal $\overline{E}$
941	$\overline{h}_e$	[m]	average erosion depth per debriton
942	$\ell$	[m]	length of runout debris, approximated as the length of the initial landslide body
943	$H/L$		the total topographic relief of the runout (measured from the center of the landslide to the
944			end of the runout path) divided by the horizontal length of the runout
945	$\kappa$	[1/m]	mean total curvature
946	$SPI$		mean specific stream power index
947	$FS$		Factor-of-Safety, ratio of the resisting to the driving forces acting on a hillslope
948			

949 **Code availability**

950 [MassWastingRunout and several tutorial notebooks area available at: https://github.com/landlab/landlab](https://github.com/landlab/landlab)

951

952 **9.0-Acknowledgements**

953 This research was partially supported by the following programs: National Science Foundation (NSF)  
 954 PREEVENTS program, ICER-1663859; NSF OAC-2103632; and NASA Grant number 22-RRNES22-  
 955 0010 and benefited from critical referee reviews. Stephen Slaughter field reviewed the Cascade  
 956 Mountains, 2009 and Black Hills landslides the year they occurred and provided photos and field  
 957 observations that aided [author](#) interpretation. John Jenkins helped with the 2022 field reconnaissance the  
 958 Cascade Mountains landslide. Eli Schwat helped with field reconnaissance at the Olympic Mountains site.  
 959 This work also benefitted from Landlab support and coding guidance from Eric Hutton and helpful  
 960 feedback from many others.

961 **10.0-Competing interests**

962 The contact author has declared that none of the authors has any competing interests.

963

964 **11.0-References**

965 Bagnold, R. A.: Experiments on a gravity-free dispersion of large solid spheres in a Newtonian fluid under shear.  
 966 Proceedings of the Royal Society of London, 225(1160), 49–63. <https://doi.org/10.1098/rspa.1954.0186>, 1954.

967 Barca, D., Crisci, G., Di Gregorio, S., and Nicoletta, F.: Cellular automata method for modelling lava flows:  
968 Simulation of the 1986–1987 eruption, Mount Etna, Sicily, in Kilburn, C., and Luongo, G., eds., *Active lavas:  
969 Monitoring and modeling*: London, University College of London Press, p. 291–309, 1993.

970 Barnhart, K. R., Hutton, E. W. H., Tucker, G. E., Gasparini, N. M., Istanbuloglu, E., Hobbey, D. E. J., Lyons, N. J.,  
971 Mouchene, M., Nudurupati, S. S., Adams, J. M., & Bandaragoda, C.: Short communication: Landlab v2.0: a software  
972 package for Earth surface dynamics. *Earth Surface Dynamics*, 8(2), 379–397. [https://doi.org/10.5194/esurf-8-379-](https://doi.org/10.5194/esurf-8-379-2020)  
973 [2020](https://doi.org/10.5194/esurf-8-379-2020), 2020.

974 Barnhart, K. R., Jones, R., George, D. J., McArdeell, B. W., Rengers, F. K., Staley, D. M., & Kean, J. W.: Multi-Model  
975 Comparison of Computed Debris Flow Runout for the 9 January 2018 Montecito, California Post-Wildfire Event.  
976 *Journal of Geophysical Research: Earth Surface*, 126(12). <https://doi.org/10.1029/2021jf006245>, 2021.

977 Benda, L., & Dunne, T.: Stochastic forcing of sediment supply to channel networks from landsliding and debris flow.  
978 *Water Resources Research*, 33(12), 2849–2863. <https://doi.org/10.1029/97wr02388>, 1997.

979 Benda, L., Veldhuisen, C. P., & Black, J.: Debris flows as agents of morphological heterogeneity at low-order  
980 confluences, Olympic Mountains, Washington. *Geological Society of America Bulletin*, 115(9), 1110.  
981 <https://doi.org/10.1130/b25265.1>, 2003.

982 Beven, K.: A manifesto for the equifinality thesis. *Journal of Hydrology*, 320(1–2), 18–36.  
983 <https://doi.org/10.1016/j.jhydrol.2005.07.007>, 2006.

984 Burton, A., & Bathurst, J. C.: Physically based modelling of shallow landslide sediment yield at a catchment scale.  
985 *Environmental Geology*, 35(2–3), 89–99. <https://doi.org/10.1007/s002540050296>, 1998.

986 Bigelow, P., Benda, L., Miller, D., & Burnett, K. M.: On Debris Flows, River Networks, and the Spatial Structure of  
987 Channel Morphology. *Forest Science*, 53(2), 220–238. <https://doi.org/10.1093/forestscience/53.2.220>, 2007

988 Campforts, B., Shobe, C. M., Overeem, I., & Tucker, G. E.: The Art of Landslides: How Stochastic Mass Wasting  
989 Shapes Topography and Influences Landscape Dynamics. *Journal of Geophysical Research: Earth Surface*, 127(8).  
990 <https://doi.org/10.1029/2022jf006745>, 2022

991 Campforts, B., Shobe, C. M., Steer, P., Vanmaercke, M., Lague, D., & Braun, J.: HyLands 1.0: a hybrid landscape  
992 evolution model to simulate the impact of landslides and landslide-derived sediment on landscape evolution.  
993 *Geoscientific Model Development*, 13(9), 3863–3886. <https://doi.org/10.5194/gmd-13-3863-2020>, 2020.

994 Capart, H., & Fraccarollo, L.: Transport layer structure in intense bed-load. *Geophysical Research Letters*, 38(20),  
995 n/a. <https://doi.org/10.1029/2011gl049408>, 2011.

996 Capart, H., Hung, C., & Stark, C. R.: Depth-integrated equations for entraining granular flows in narrow channels.  
997 *Journal of Fluid Mechanics*, 765. <https://doi.org/10.1017/jfm.2014.713>, 2015.

998 Carretier, S., Martinod, P., Reich, M., & Godd ris, Y.: Modelling sediment clasts transport during landscape evolution.  
999 *Earth Surface Dynamics*, 4(1), 237–251. <https://doi.org/10.5194/esurf-4-237-2016>, 2016.

1000 Chase, C. G.: Fluvial landsculpting and the fractal dimension of topography. *Geomorphology*, 5(1–2), 39–57.  
1001 [https://doi.org/10.1016/0169-555x\(92\)90057-u](https://doi.org/10.1016/0169-555x(92)90057-u), 1992.

1002 Chen, C., & Yu, F.: Morphometric analysis of debris flows and their source areas using GIS. *Geomorphology*, 129(3–  
1003 4), 387–397. <https://doi.org/10.1016/j.geomorph.2011.03.002>, 2011.

1004 Chen, H., & Zhang, L.: EDDA 1.0: integrated simulation of debris flow erosion, deposition and property changes.  
1005 *Geoscientific Model Development*, 8(3), 829–844. <https://doi.org/10.5194/gmd-8-829-2015>, 2015.

1006 Chen, T.-Y. K., Wu, Y.-C., Hung, C.-Y., Capart, H., and Voller, V. R.: A control volume finite-element model for  
1007 predicting the morphology of cohesive-frictional debris flow deposits, *Earth Surface Dynamics*, 11, 325–342,  
1008 <https://doi.org/10.5194/esurf-11-325-2023>, 2023.

1009 Clerici, A., & Perego, S.: Simulation of the Parma River blockage by the Corniglio landslide (Northern Italy).  
1010 *Geomorphology*, 33(1–2), 1–23. [https://doi.org/10.1016/s0169-555x\(99\)00095-1](https://doi.org/10.1016/s0169-555x(99)00095-1), 2000.

1011 Codd, E. F.: *Cellular Automata* (1st ed.). New York, Academic Press, 1968.

1012 Coz, J. L., Renard, B., Bonnifait, L., Branger, F., & Boursicaud, R. L.: Combining hydraulic knowledge and uncertain  
1013 gaugings in the estimation of hydrometric rating curves: A Bayesian approach. *Journal of Hydrology*, 509, 573–587.  
1014 <https://doi.org/10.1016/j.jhydrol.2013.11.016>, 2014.

1015 Crave, A., & Davy, P.: A stochastic “precipiton” model for simulating erosion/sedimentation dynamics. *Computers  
1016 & Geosciences*, 27(7), 815–827. [https://doi.org/10.1016/s0098-3004\(00\)00167-9](https://doi.org/10.1016/s0098-3004(00)00167-9), 2001.

1017 D’Ambrosio, D., Di Gregorio, S., Iovine, G., Lupiano, V., Rongo, R., & Spataro, W.: First simulations of the Sarno  
1018 debris flows through Cellular Automata modelling. *Geomorphology*, 54(1–2), 91–117. [https://doi.org/10.1016/s0169-555x\(03\)00058-8](https://doi.org/10.1016/s0169-555x(03)00058-8), 2003.

1020 Egashira, S., Honda, N., & Itoh, T.: Experimental study on the entrainment of bed material into debris flow. *Physics  
1021 and Chemistry of the Earth, Parts a/B/C*, 26(9), 645–650. [https://doi.org/10.1016/s1464-1917\(01\)00062-9](https://doi.org/10.1016/s1464-1917(01)00062-9), 2001.

1022 Foglia, L., Hill, M. C., Mehl, S. W., and Burlando, P. (2009), Sensitivity analysis, calibration, and testing of a  
1023 distributed hydrological model using error-based weighting and one objective function, *Water Resources  
1024 Research*, 45, W06427, doi:10.1029/2008WR007255.

1025 Fannin, R. J., & Wise, M. P.: An empirical-statistical model for debris flow travel distance. *Canadian Geotechnical  
1026 Journal*, 38(5), 982–994. <https://doi.org/10.1139/t01-030>, 2001.

1027 Frank, F., McArdell, B. W., Huggel, C., & Vieli, A.: The importance of entrainment and bulking on debris flow runout  
1028 modeling: examples from the Swiss Alps. *Natural Hazards and Earth System Sciences*, 15(11), 2569–2583.  
1029 <https://doi.org/10.5194/nhess-15-2569-2015>, 2015.

1030 Freeman, T. G.: Calculating catchment area with divergent flow based on a regular grid. *Computers &  
1031 Geosciences*, 17(3), 413–422. [https://doi.org/10.1016/0098-3004\(91\)90048-i](https://doi.org/10.1016/0098-3004(91)90048-i), 1991.



1032 Gartner, J. E., Cannon, S. H., & Santi, P. M.: Empirical models for predicting volumes of sediment deposited by debris  
1033 flows and sediment-laden floods in the transverse ranges of southern California. *Engineering Geology*, 176, 45–56.  
1034 <https://doi.org/10.1016/j.enggeo.2014.04.008>, 2014.

1035 Gelman, A., Carlin, J. B., Stern, H. S., Dunson, D. B., Vehtari, A., & Rubin, D. B.: *Bayesian Data Analysis* (3rd ed.).  
1036 Electronic Edition, 2021.

1037 Goode, J. R., Luce, C. H., & Buffington, J. M.: Enhanced sediment delivery in a changing climate in semi-arid  
1038 mountain basins: Implications for water resource management and aquatic habitat in the northern Rocky Mountains.  
1039 *Geomorphology*, 139–140, 1–15. <https://doi.org/10.1016/j.geomorph.2011.06.021>, 2012.

1040 Gorr, A., McGuire, L. A., Youberg, A., & Rengers, F. K.: A progressive flow-routing model for rapid assessment of  
1041 debris-flow inundation. *Landslides*, 19(9), 2055–2073. <https://doi.org/10.1007/s10346-022-01890-y>, 2022

1042 Guthrie, R., Hockin, A., Colquhoun, L., Nagy, T., Evans, S. G., & Ayles, C. P.: An examination of controls on debris  
1043 flow mobility: Evidence from coastal British Columbia. *Geomorphology*, 114(4), 601–613.  
1044 <https://doi.org/10.1016/j.geomorph.2009.09.021>, 2010.

1045 Guthrie, R. H., & Befus, A. D.: DebrisFlow Predictor: an agent-based runout program for shallow landslides. *Natural*  
1046 *Hazards and Earth System Sciences*, 21(3), 1029–1049. <https://doi.org/10.5194/nhess-21-1029-2021>, 2021.

1047 Hammond C.J., Prellwitz R.W., Miller S.M.: Landslides hazard assessment using Monte Carlo simulation. In: Bell  
1048 DH (ed) *Proceedings of 6th international symposium on landslides*, Christchurch, New Zealand, Balkema, vol 2. pp  
1049 251–294, 1992.

1050 Han, Z., Chen, G., Li, Y., Tang, C., Xu, L., He, Y., Huang, X., & Wang, W.: Numerical simulation of debris-flow  
1051 behavior incorporating a dynamic method for estimating the entrainment. *Engineering Geology*, 190, 52–64.  
1052 <https://doi.org/10.1016/j.enggeo.2015.02.009>, 2015.

1053 Han, Z., Li, Y., Huang, J., Chen, G., Xu, L., Tang, C. Y., Zhang, H., & Shang, Y.: Numerical simulation for run-out  
1054 extent of debris flows using an improved cellular automaton model. *Bulletin of Engineering Geology and the*  
1055 *Environment*, 76(3), 961–974. <https://doi.org/10.1007/s10064-016-0902-6>, 2017.

1056 Han, Z., Ma, Y., Li, Y., Zhang, H., Chen, N., Hu, G., & Chen, G.: Hydrodynamic and topography based cellular  
1057 automaton model for simulating debris flow run-out extent and entrainment behavior. *Water Research*, 193, 116872.  
1058 <https://doi.org/10.1016/j.watres.2021.116872>, 2021.

1059 Heiser, M., Scheidl, C., & Kaitna, R.: Evaluation concepts to compare observed and simulated deposition areas of  
1060 mass movements. *Computational Geosciences*, 21(3), 335–343. <https://doi.org/10.1007/s10596-016-9609-9>, 2017.

1061 Hobley, D. E. J., Adams, J. M., Nudurupati, S. S., Hutton, E. W. H., Gasparini, N. M., Istanbuluoglu, E., & Tucker,  
1062 G. E.: Creative computing with Landlab: an open-source toolkit for building, coupling, and exploring two-dimensional  
1063 numerical models of Earth-surface dynamics. *Earth Surface Dynamics*, 5(1), 21–46. [https://doi.org/10.5194/esurf-5-](https://doi.org/10.5194/esurf-5-21-2017)  
1064 [21-2017](https://doi.org/10.5194/esurf-5-21-2017), 2017.

1065 [Holmgren, P.: Multiple flow direction algorithms for runoff modelling in grid based elevation models: An empirical](#)  
1066 [evaluation. \*Hydrological Processes\*, 8\(4\), 327–334. <https://doi.org/10.1002/hyp.3360080405>, 1994](#)

1067 Horton, P., Jaboyedoff, M., Rudaz, B., & Zimmermann, M. N.: Flow-R, a model for susceptibility mapping of debris  
1068 flows and other gravitational hazards at a regional scale. *Natural Hazards and Earth System Sciences*, 13(4), 869–885.  
1069 <https://doi.org/10.5194/nhess-13-869-2013>, 2013.

1070 Hungr, O., Morgan, G. J., & Kellerhals, R.: Quantitative analysis of debris torrent hazards for design of remedial  
1071 measures. *Canadian Geotechnical Journal*, 21(4), 663–677. <https://doi.org/10.1139/t84-073>, 1984.

1072 Hungr, O., & Evans, S. G.: Entrainment of debris in rock avalanches: An analysis of a long run-out mechanism.  
1073 *Geological Society of America Bulletin*, 116(9), 1240. <https://doi.org/10.1130/b25362.1>, 2004.

1074 Hutter, K., Svendsen, B., & Rickenmann, D.: Debris flow modeling: A review. *Continuum Mechanics and*  
1075 *Thermodynamics*, 8(1), 1–35. <https://doi.org/10.1007/bf01175749>, 1996.

1076 Iovine, G., D’Ambrosio, D., & Di Gregorio, S.: Applying genetic algorithms for calibrating a hexagonal cellular  
1077 automata model for the simulation of debris flows characterised by strong inertial effects. *Geomorphology*, 66(1–4),  
1078 287–303. <https://doi.org/10.1016/j.geomorph.2004.09.017>, 2005.

1079 Istanbuluoglu, E. Bras R. L.: Vegetation-modulated landscape evolution: Effects of vegetation on landscape  
1080 processes, drainage density, and topography. *Journal of Geophysical Research*, 110(F2).  
1081 <https://doi.org/10.1029/2004jf000249>, 2005.

1082 Istanbuluoglu, E., Bras R. L., Flores-Cervantes, H., and Tucker, G. E.: Implications of bank failures and fluvial  
1083 erosion for gully development: Field observations and modeling, *J. Geophysical Research*, 110, F01014,  
1084 [doi:10.1029/2004JF000145](https://doi.org/10.1029/2004JF000145), 2005.

1085 Istanbuluoglu, E., O. Yetemen, E. R. Vivoni, H. A. Gutierrez-Jurado, and R. L. Bras, Eco-geomorphic implications  
1086 of hillslope aspect: Inferences from analysis of landscape morphology in central New Mexico, *Geophysical. Research*  
1087 *Letters*, 35, L14403, [10.1029/2008GL034477](https://doi.org/10.1029/2008GL034477), 2008.

1088 Iverson, R. M.: The physics of debris flows. *Reviews of Geophysics*, 35(3), 245–296.  
1089 <https://doi.org/10.1029/97rg00426>, 1997.

1090 Iverson, R. M., & Denlinger, R. P.: Flow of variably fluidized granular masses across three-dimensional terrain: 1.  
1091 Coulomb mixture theory. *Journal of Geophysical Research*, 106(B1), 537–552.  
1092 <https://doi.org/10.1029/2000jb900329>, 2001.

1093 Iverson, R.M., How should mathematical models of geomorphic processes be judged?. In Wilcock, P., & Iverson, R.  
1094 (Eds.), *Prediction in Geomorphology*. American Geophysical Union, 2003.

1095 Julien, P. Y., & Paris, A.: Mean Velocity of Mudflows and Debris Flows. *Journal of Hydraulic Engineering*, 136(9),  
1096 676–679. [https://doi.org/10.1061/\(asce\)hy.1943-7900.0000224](https://doi.org/10.1061/(asce)hy.1943-7900.0000224), 2010.

1097 Kean, J. W., Staley, D. M., Lancaster, J., Rengers, F., Swanson, B., Coe, J., et al.: Inundation, flow dynamics, and  
1098 damage in the 9 January 2018 Montecito debris-flow event, California, USA: Opportunities and challenges for post-  
1099 wildfire risk assessment. *Geosphere*, 15(4), 1140–1163. <https://doi.org/10.1130/GES02048.1>, 2019

1100 Korup, O.: Effects of large deep-seated landslides on hillslope morphology, western Southern Alps, New Zealand.  
1101 *Journal of Geophysical Research*, 111(F1). <https://doi.org/10.1029/2004jf000242>, 2006

1102 Lancaster, S. T., Hayes, S. K., & Grant, G. E.: Effects of wood on debris flow runout in small mountain watersheds.  
1103 *Water Resources Research*, 39(6). <https://doi.org/10.1029/2001wr001227>, 2003.

1104 Larsen, I. J., & Montgomery, D. R.: Landslide erosion coupled to tectonics and river incision. *Nature Geoscience*,  
1105 5(7), 468–473. <https://doi.org/10.1038/ngeo1479>, 2012.

1106 Liu, J., Wu, Y., Gao, X., & Zhang, X.: A Simple Method of Mapping Landslides Runout Zones Considering Kinematic  
1107 Uncertainties. *Remote Sensing*, 14(3), 668. <https://doi.org/10.3390/rs14030668>, 2022.

1108 Major, J. J.: Depositional Processes in Large-Scale Debris-Flow Experiments. *The Journal of Geology*, 105(3), 345–  
1109 366. <https://doi.org/10.1086/515930>, 1997.

1110 Major, J. J., & Iverson, R. M.: Debris-flow deposition: Effects of pore-fluid pressure and friction concentrated at flow  
1111 margins. *Geological Society of America Bulletin*, 111(10), 1424–1434. [https://doi.org/10.1130/0016-7606\(1999\)111](https://doi.org/10.1130/0016-7606(1999)111),  
1112 1999.

1113 McCoy, S. W., Kean, J. W., Coe, J. A., Tucker, G. S., Staley, D. M., & Wasklewicz, T. A.: Sediment entrainment by  
1114 debris flows: In situ measurements from the headwaters of a steep catchment. *Journal of Geophysical Research*,  
1115 117(F3), n/a. <https://doi.org/10.1029/2011jf002278>, 2012.

1116 McDougall, S., & Hungr, O.: A model for the analysis of rapid landslide motion across three-dimensional terrain.  
1117 *Canadian Geotechnical Journal*, 41(6), 1084–1097. <https://doi.org/10.1139/t04-052>, 2004.

1118 Medina, V., Hürlimann, M., & Bateman, A.: Application of FLATModel, a 2D finite volume code, to debris flows in  
1119 the northeastern part of the Iberian Peninsula. *Landslides*, 5(1), 127–142. [https://doi.org/10.1007/s10346-007-0102-](https://doi.org/10.1007/s10346-007-0102-3)  
1120 [3](https://doi.org/10.1007/s10346-007-0102-3), 2008.

1121 Montgomery, D. R., & Dietrich, W. E.: Where do channels begin? *Nature*, 336(6196), 232–234.  
1122 <https://doi.org/10.1038/336232a0>, 1988.

1123 Murray, B.A., & Paola, C.: A cellular model of braided rivers. *Nature*, 371(6492), 54–57.  
1124 <https://doi.org/10.1038/371054a0>, 1994.

1125 Murray, A. B., & Paola, C.: Properties of a cellular braided-stream model. *Earth Surface Processes and Landforms*,  
1126 22(11), 1001–1025. [https://doi.org/10.1002/\(sici\)1096-9837\(199711\)22:11](https://doi.org/10.1002/(sici)1096-9837(199711)22:11), 1997.  
1127

1128 Murray A.B.: Which Models Are Good (Enough), and When?. In: John F. Shroder (ed.) *Treatise on Geomorphology*,  
1129 Volume 2, pp. 50-58. San Diego: Academic Press, 2013.

1130 Natural Resources Conservation Service | Snow and Water Interactive Map (n.d.). Natural Resources Conservation  
1131 Service. <https://www.nrcs.usda.gov/resources/data-and-reports/snow-and-water-interactive-map>, Accessed April,  
1132 2022

1133 Nudurupati, S. S., Istanbuluoglu, E., Tucker, G. E., Gasparini, N. M., Hobley, D. E. J., Hutton, E. W. H., Barnhart,  
1134 K. R., & Adams, J. M.: On transient semi-arid ecosystem dynamics using Landlab: vegetation shifts, topographic  
1135 refugia, and response to climate. *Water Resources Research*, 59(4). <https://doi.org/10.1029/2021wr031179>, 2023.

1136 Perron, J. T.: Climate and the Pace of Erosional Landscape Evolution. *Annual Review of Earth and Planetary Sciences*,  
1137 45(1), 561–591. <https://doi.org/10.1146/annurev-earth-060614-105405>, 2017.

1138 Reid, M. J., Coe, J. A., & Brien, D. L.: Forecasting inundation from debris flows that grow volumetrically during  
1139 travel, with application to the Oregon Coast Range, USA. *Geomorphology*, 273, 396–411.  
1140 <https://doi.org/10.1016/j.geomorph.2016.07.039>, 2016.

1141 Renard, B., Garreta, V., & Lang, M. J.: An application of Bayesian analysis and Markov chain Monte Carlo methods  
1142 to the estimation of a regional trend in annual maxima. *Water Resources Research*, 42(12).  
1143 <https://doi.org/10.1029/2005wr004591>, 2006.

1144 Rengers, F. K., McGuire, L. A., Kean, J. W., Staley, D. M., and Hobley, D. E. J.: Model simulations of flood and  
1145 debris flow timing in steep catchments after wildfire, *Water Resources Research*, 52, 6041–6061,  
1146 doi:10.1002/2015WR018176, 2016.

1147 Roda-Boluda, D. C., D’Arcy, M., McDonald, J., & Whittaker, A. C.: Lithological controls on hillslope sediment  
1148 supply: insights from landslide activity and grain size distributions. *Earth Surface Processes and Landforms*, 5), 956–  
1149 977. <https://doi.org/10.1002/esp.4281>, 2018.

1150 Shaller, P. J., Doroudian, M., & Hart, M. W.: The Eureka Valley Landslide: Evidence of a dual failure mechanism for  
1151 a Long-Runout Landslide. *Lithosphere*, 2020(1). <https://doi.org/10.2113/2020/8860819>, 2020.

1152 Schürch, P., Densmore, A. L., Rosser, N., & McArdell, B. W.: Dynamic controls on erosion and deposition on debris-  
1153 flow fans. *Geology*, 39(9), 827–830. <https://doi.org/10.1130/g32103.1>, 2011.

1154 Shen, P., Zhang, L. M., Wong, H., Peng, D., Zhou, S., Zhang, S., & Chen, C.: Debris flow enlargement from  
1155 entrainment: A case study for comparison of three entrainment models. *Engineering Geology*, 270, 105581.  
1156 <https://doi.org/10.1016/j.enggeo.2020.105581>, 2020.

1157 Stock, J. P. J., & Dietrich, W. E.: Erosion of steepland valleys by debris flows. *Geological Society of America Bulletin*,  
1158 118(9–10), 1125–1148. <https://doi.org/10.1130/b25902.1>, 2006.



1159 Strauch, R. L., Istanbuluoglu, E., Nudurupati, S. S., Bandaragoda, C., Gasparini, N. M., & Tucker, G. E.: A  
1160 hydroclimatological approach to predicting regional landslide probability using Landlab. *Earth Surface Dynamics*,  
1161 6(1), 49–75. <https://doi.org/10.5194/esurf-6-49-2018>, 2018.

1162 Takahashi, T.: *Debris Flow* (2nd ed.). CRC Press, Taylor & Francis Group, 2014.

1163 Tucker, G. E., & Bras, R. L.: Hillslope processes, drainage density, and landscape morphology. *Water Resources*  
1164 *Research*, 34(10), 2751–2764. <https://doi.org/10.1029/98wr01474>, 1998.

1165 Tucker, G. E., Hancock, G. J.: Modelling landscape evolution. *Earth Surface Processes and Landforms*, 35(1), 28–50.  
1166 <https://doi.org/10.1002/esp.1952>, 2010.

1167 Tucker, G. E., McCoy, S., & Hobley, D. E. J.: A lattice grain model of hillslope evolution. *Earth Surface Dynamics*,  
1168 6(3), 563–582. <https://doi.org/10.5194/esurf-6-563-2018>, 2018.

1169 Western Regional Climate Center. (n.d.), from <https://wrcc.dri.edu/>, accessed 2017 and 2022

1170 Whipple, K. X., & Dunne, T.: The influence of debris-flow rheology on fan morphology, Owens Valley, California.  
1171 *Geological Society of America Bulletin*, 104(7), 887–900. [https://doi.org/10.1130/0016-7606\(1992\)104](https://doi.org/10.1130/0016-7606(1992)104), 1992.

1172 Zhou, G. G. D., Li, S., Song, D., Choi, C. E., & Chen, X.: Depositional mechanisms and morphology of debris flow:  
1173 physical modelling. *Landslides*, 16(2), 315–332. <https://doi.org/10.1007/s10346-018-1095-9>, 2019.

1174

1175